European Journal of Mechanics / A Solids 93 (2022) 104547

Contents lists available at ScienceDirect

European Journal of Mechanics / A Solids

journal homepage: www.elsevier.com/locate/ejmsol

Adaptive Gaussian Process with PCA for prediction of complex dispersion relations for periodic structures

Zhibao Cheng [a], Min Li [b], Gaofeng Jia [b,*], Zhifei Shi [a]

[a] School of Civil Engineering, Beijing Jiaotong University, Beijing, 100044, China
[b] Department of Civil and Environmental Engineering, Colorado State University, Fort Collins, CO, 80523, USA

ARTICLE INFO

Keywords:
Complex dispersion relations
Periodic structures
Adaptive Gaussian process
Surrogate model
Uncertainty quantification
Principal component analysis

ABSTRACT

The complex dispersion relation is important for understanding the wave propagation in periodic structures. However, its calculation is much more expensive compared to calculation of the real dispersion relation, due to the need to solve the dispersion equation at large number of frequencies. For uncertainty quantification in the dispersion relations, the computational challenge is even higher. This paper proposes an adaptive Gaussian process (AGP) model to efficiently predict the complex dispersion relations for periodic structures with different properties. Instead of directly building GP for the dispersion relation, which is challenging due to discontinuity in the dispersion relation, we first reformulate the problem as predicting the coefficients of the dispersion equation at selected frequencies, where these coefficients are continuous and smooth functions of the properties of periodic structures. Then GP model is trained to predict these coefficients, based on which the dispersion equation is then analytically solved to establish the complex dispersion relation. Second, Principal component analysis (PCA) is used to reduce the dimension of these coefficients to facilitate efficient training of GP model. Third, an adaptive procedure is integrated to iteratively add training data that can most effectively improve the GP model accuracy. Results verify the great efficiency and accuracy of the proposed approach for both undamped and damped periodic structures. The proposed approach has great promise in improving efficiency for uncertainty quantification, sensitivity analysis, and design optimization of periodic structures.

1. Introduction

In the last two decades, the research on elastic wave propagation in artificial periodic structures, known as phononic crystals or elastic metamaterials, has drawn the attention of many scientists and engineers due to their special properties such as negative density, negative refraction, and so on. These special properties have many potential engineering applications. With proper design, periodic structures could be fabricated to prohibit elastic waves in certain frequency regions, which gives a new way to design the sound-proof materials and vibration isolation structures in civil and mechanical engineering (Chen et al., 2017; Xiao and Wen, 2020; Cheng and Shi, 2013b; Gao and Lu, 2020; Zhou et al., 2019; Yao et al., 2020). In particular, to attenuate the harmful seismic responses of engineering structures, different types of large-scale periodic structures, named periodic foundation(or meta-foundation) and periodic wave barriers (or meta-barriers), have been proposed (Jia and Shi, 2010; Cheng and Shi, 2013b; Dertimanis et al., 2016; Palermo et al., 2018; Cheng et al., 2020; Wenzel et al., 2020).

To investigate the special dynamic properties of periodic structures, one important way is to solve the dispersion equation, which is an implicit function $\mathbb{F}$ between the wave number ($k = k_\alpha + \mathrm{i}k_\beta$) and frequency number ($\omega$). Ignoring the imaginary part of the wave number, dispersion equation $\mathbb{F}(\omega, k)$ can be given as an eigenvalue equation with respect to the frequency ω. For a given real wave number k_α, ω can be obtained easily by performing the mode analysis, which is the widely used $\omega(k_\alpha)$ method. Dispersion relation obtained by the $\omega(k_\alpha)$ method corresponds to *real dispersion relation*, which only includes dispersion properties of propagative waves. Indeed, dispersion equation $\mathbb{F}(\omega, k)$ can also be solved by seeking the complex wave number k for given real frequencies ω, which is the so-called $k(\omega)$ method. Interestingly, the complex wave number $k = k_\alpha + \mathrm{i}k_\beta$ includes all possible waves, propagative wave as well as evanescent waves, into the dispersion relation. Therefore, dispersion relation obtained by the $k(\omega)$ method is named *complex dispersion relation*.

To analyze the wave attenuation properties (i.e., the evanescent wave properties) for the damped and undamped periodic structures, the $k(\omega)$ method must be used. However, it must be pointed out that because the complex wave number is considered, computational effort of the $k(\omega)$ method is much larger than that of the $\omega(k)$ method. Thus,

* Corresponding author.
E-mail address: Gaofeng.Jia@colostate.edu (G. Jia).

https://doi.org/10.1016/j.euromechsol.2022.104547
Received 2 May 2021; Received in revised form 25 October 2021; Accepted 31 January 2022
Available online 12 February 2022

only a few $k(\omega)$ numerical methods are reported (Laude et al., 2009; Veres and Berer, 2012; Xiao et al., 2012; Cheng et al., 2017, 2018). For instances, the widely used $\omega(k_\alpha)$ method, the plane wave expansion (PWE) method, was modified by Laude et al. (2009) to calculate the complex band structure of a two-dimensional periodic structure. However, the PWE encounters convergence problems especially when the material mismatch of the unit cell is large (Cheng and Shi, 2013a). To overcome such problem, the Wave Finite Element Method (WFEM) was developed (Mace et al., 2005; Mace and Manconi, 2008; Veres and Berer, 2012). The WFEM can handle periodic structure of any shape and its computational requirement is relatively large. To eliminate this drawback, the Component Mode Synthesis (CMS) was recently introduced to improve the WFEM (Palermo et al., 2018; Thierry et al., 2018). Recently, Cheng et al. (2018) developed the extended differential quadrature element method (EDQEM) and investigated the complex dispersion relations of periodic beams. Tang et al. (2021) employed the method of the reverberation-ray matrix (MRRM) to provide better physical understanding of flexural wavenumber spectral behaviors of the beam coupled with periodic resonators. Furthermore, calculation of the complex dispersion relations at large number of frequencies with fine frequency resolutions (e.g., tens of thousands of frequencies) requires repeated solution of the dispersion equation, which entails significant computational effort. Therefore, so far investigations about the complex dispersion relations are still limited.

In addition, in practice there are various uncertainties related to the physical and geometrical parameters of the periodic structures. Understanding how these uncertainties affect the dispersion relations and the resultant bandgap characteristics is critical for understanding the behavior the periodic structures and for designing periodic structures with targeted performances that are robust to uncertainties. For these purposes, typically uncertainty propagation, or sensitivity analysis, or design optimization under uncertainty needs to be carried out. Stochastic simulation techniques (such as Monte Carlo Simulation (MCS)) can be used. However, they typically require large number of model evaluations. Therefore, direct calculation of the complex dispersion relations in the context of using stochastic simulation for uncertainty propagation entails huge computational effort.

On the other hand, surrogate models have been used to address the computational challenges when many model evaluations are needed and the system models are expensive to evaluate (Sacks et al., 1989; Simpson et al., 2001; Forrester et al., 2008). Surrogate models are mathematical representations used to efficiently approximate the input–output relationships for expensive system models. Surrogate models are usually built/trained based on a small number of runs of the system model. Once trained, they can be used to efficiently predict the system outputs for new inputs that are not in the training set. Various surrogate models have been used in the literature, for example, polynomial response surfaces (Jones, 2001; Breitkopf et al., 2005; Taflanidis et al., 2013), artificial neural networks, support vector machines (Bourinet et al., 2011; Moustapha et al., 2018), polynomial chaos expansions (Sudret, 2008; Yaghoubi et al., 2017; Schneider et al., 2020), and kriging (also known as Gaussian process model) (Rasmussen and Williams, 2006; Jia and Taflanidis, 2013; Jia et al., 2016; Lu et al., 2019; Li and Jia, 2020). Among them, Gaussian process model has been gaining popularity due to its flexibility in modeling complex functions and also the ability to provide not only the mean prediction but also the local variance of the prediction (Rasmussen and Williams, 2006; Zhang et al., 2017, 2018; Li et al., 2019; Kyprioti et al., 2020). For system model with high-dimensional outputs, it is typically computationally prohibitive to train a surrogate model for each individual output. To address this, dimension reduction or sparse representation techniques have also been proposed in the literature (Jia and Taflanidis, 2013; Blatman and Sudret, 2010; Marelli and Sudret, 2015; Jia et al., 2016; Li et al., 2020).

To address the challenges in prediction and uncertainty quantification for the complex dispersion relations, this paper proposes an adaptive Gaussian process (AGP) model to efficiently predict the complex dispersion relations for periodic structures with different properties. The idea of using GP model to predict the complex dispersion is novel. So far, investigations on the complex dispersion relation of periodic structure are very limited because of the computational difficulty. Few methods were developed and the computational requirement of these methods is typically high, especially when uncertainty quantification is considered. The use of GP model can significantly improve the computational efficiency of carrying out the above analyses. Several novel aspects are proposed and integrated to improve accuracy and efficiency of the proposed approach. First, the problem is reformulated by choosing proper inputs and output for the GP model to address the discontinuity in the output to improve the accuracy of the established GP model. Instead of directly building GP for the dispersion relation, which is challenging due to the discontinuity in the dispersion relation, we first build GP to predict the coefficients of the dispersion equation (at selected frequencies), which are continuous and smooth functions of the properties of the periodic structures. Second, Principal component analysis (PCA) is used to reduce the dimension of these coefficients (which correspond to high-dimensional outputs) and then the GP model is efficiently trained with respect to the low-dimensional latent outputs. Based on the predicted coefficients by GP model, the dispersion equation is then analytically solved to establish the complex dispersion relations. In addition, an adaptive procedure using weighted accumulative errors is integrated to iteratively add training data to effectively improve the GP model accuracy. The overall proposed approach is named as AGP-PCA. The efficiency and accuracy of the proposed approach are verified through prediction and uncertainty quantification of the complex dispersion relations and bandgap characteristics for periodic beams where the training data is established by the EDQEM.

The remainder of this paper is organized as follows. Section 2 presents the complex wave dispersion problem for periodic structures and discusses the computational challenges in predicting the complex dispersion relations and in quantifying the uncertainties in the complex dispersion relations. Section 3 presents the proposed AGP-PCA approach for efficient prediction of complex dispersion relations of periodic structures. Section 4 presents the illustrative example with application to periodic beams, and discusses the performances (e.g., accuracy and efficiency) of the proposed approach in predicting the complex dispersion relations, where both the case without damping and the case with damping are investigated. Section 5 presents further applications of the established AGP-PCA approach to facilitate efficient uncertainty quantification and parametric study for the complex dispersion relations and bandgap characteristics of periodic beams. Finally, Section 6 summarizes the research findings.

2. Problem formulation

2.1. Dispersion equations and complex dispersion relations

Complex dispersion problem for the flexural wave propagating in a periodic Timoshenko beam structure, shown in Fig. 1(a), is considered. The periodic beam structure consists of two materials: material 1 of length L_1 and material 2 of length L_2. The lattice constant is $L = L_1 + L_2$. E_m, G_m and ρ_m are the Young's modulus, shear modulus and density per volume of material m ($m = 1, 2$). A_m and I_m are the cross-sectional area and area moment of inertia with respect to the z axis of material m.

Governing equations of the considered system are

$$\begin{cases} \kappa_m \mathrm{G}_m A_m \left(\varphi_m(x,t) - \frac{\partial v_m(x,t)}{\partial x}\right) - \mathrm{E}_m I_m \frac{\partial^2 \varphi_m(x,t)}{\partial x^2} + \rho_m I_m \frac{\partial^2 \varphi_m(x,t)}{\partial t^2} = 0 \\ \frac{\partial}{\partial x}\left[\kappa_m \mathrm{G}_m A_m \left(\varphi_m(x,t) - \frac{\partial v_m(x,t)}{\partial x}\right)\right] + \rho_m A_m \frac{\partial^2 v_m(x,t)}{\partial t^2} = 0 \end{cases} \quad (1)$$

in which $v(x,t)$ is the transverse deflection, $\varphi(x,t)$ is the rotation angle; $\kappa = 5/6$ is the shear correction coefficient. By using the Bloch–Floquet theorem, the displacement field can be expressed as $\mathbf{u}(x,t) = \mathbf{u}_k(x)\mathrm{e}^{\mathrm{i}(k\cdot x - \omega t)}$. Here $\mathrm{i} = \sqrt{-1}$, k is the wave number. In particular,

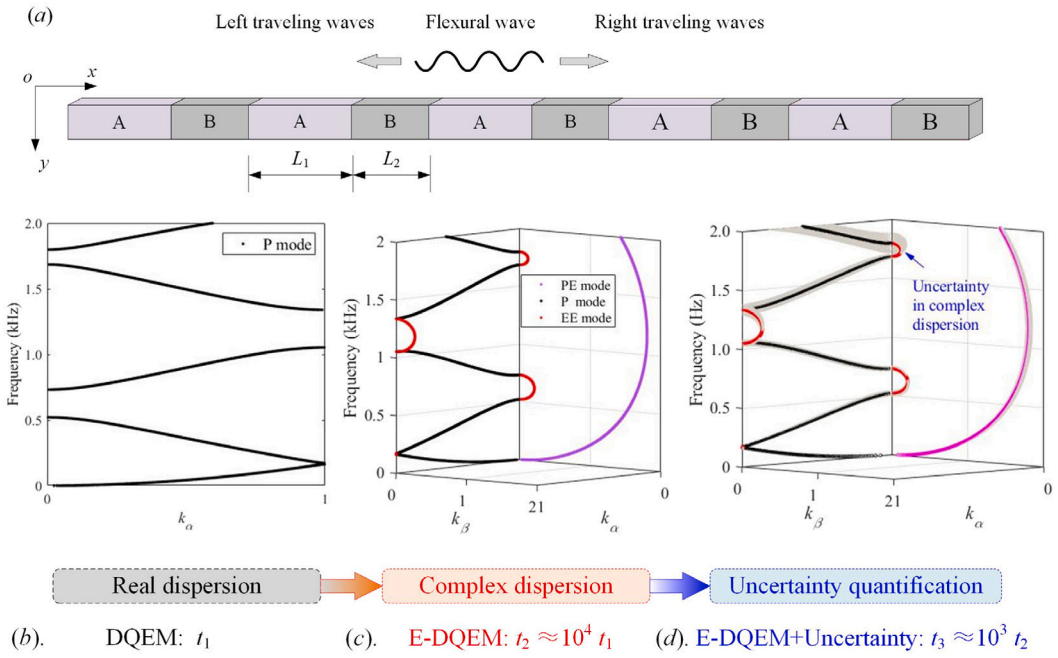

Fig. 1. Illustration of (a) an infinite periodic Timoshenko beam, and the computational requirements for its (b) real dispersion, (c) complex dispersion and (d) uncertainty quantification in complex dispersion.

$\mathbf{u}_k(x)$ is a periodic function with the same periodicity as the unit cell, $\mathbf{u}_k(x+L) = \mathbf{u}_k(x)$. As such, the relations between the two ends of the unit cell can be given as $\mathbf{u}(x+L,t) = e^{\mathrm{i}k\cdot L}\mathbf{u}(x,t)$, which is the so-called *periodic boundary condition*.

Further, coupling the wave equation (Eq. (1)) and the periodic boundary condition, the dispersion problem of the infinite domain will be transferred into an eigenvalue problem of a finite domain, which can be given as

$$\mathbf{D}(\omega;k)\mathbf{U} = (\mathbf{\Phi}(k) - \omega^2\mathbf{M})\mathbf{U} = \mathbf{0} \tag{2}$$

in which $\mathbf{\Phi}$ and $\mathbf{M}$ are the stiffness and mass matrix of the system, respectively. $\mathbf{D}(\omega;k)$ is the reduced dynamic stiffness matrix. $\mathbf{U} = (V,\psi)$ is the displacement vector, $V(x)$ and $\psi(x)$ are the steady-state responses of $v(x,t)$ and $\varphi(x,t)$, respectively.

When the viscous material damping or structural damping is included, the dynamic stiffness matrix $\mathbf{D}(\omega;k)$ can be modified by the addition of the viscous or structural damping matrices as (Mace and Manconi, 2008)

$$\mathbf{D}(\omega;k) = (\mathbf{\Phi} + \mathrm{i}\mathbf{\Phi}') - \omega^2\mathbf{M}, \quad \mathbf{D}(\omega;k) = \mathbf{\Phi} + \mathrm{i}\omega\mathbf{C} - \omega^2\mathbf{M} \tag{3}$$

in which $\mathbf{\Phi}'$ and $\mathbf{C}$ are the viscous damping matrix and the structural damping matrix, respectively.

Eq. (2) is the so-called *dispersion equation*, which can be solved by using the $\omega(k_\alpha)$ method or the $k(\omega)$ method. As using the traditional $\omega(k_\alpha)$ strategy, only the real wave number k_α is considered. And, the dispersion relation, i.e., the real dispersion relation, can only indicate dispersion properties of propagative waves (P mode in Fig. 1b). On the other hand, if using the $k(\omega)$ strategy, the wave number k will be a complex number $k = k_\alpha + \mathrm{i}k_\beta$. Here, k_β represents dispersion properties (i.e., the attenuation properties) of the evanescent wave. As shown in Fig. 1c, except for the propagative wave mode, another two evanescent wave modes, i.e., the purely evanescent wave mode (PE mode) and the evanescent edge wave mode (EE mdoe), are observed in the considered frequency region (Cheng et al., 2018). These properties are missed in the real dispersion curves. However, because the evanescent wave mode is included, computational effort of the $k(\omega)$ strategy is much larger than that of the $\omega(k_\alpha)$ method. Only a few $k(\omega)$ numerical methods are reported (Laude et al., 2009; Veres and Berer, 2012; Xiao et al., 2012; Cheng et al., 2017, 2018).

2.2. Differential-quadrature approximation based methods

The Extended Differential Quadrature Element Method was recently developed to calculate the complex dispersion relation of periodic structures (Cheng et al., 2018). Within the EDQEM, the dispersion equations can be written more explicitly as

$$\begin{bmatrix} \mathbf{\Phi}_{DD} - \omega^2\mathbf{M}_D & \mathbf{\Phi}_{DI} & \mathbf{\Phi}_{DP} \\ \mathbf{\Phi}_{ID} & \mathbf{\Phi}_{II} & \mathbf{\Phi}_{IP} \\ \mathbf{\Phi}_{PD}(\lambda) & \mathbf{\Phi}_{PI}(\lambda) & \mathbf{\Phi}_{PP}(\lambda) \end{bmatrix} \begin{bmatrix} \mathbf{U}_D \\ \mathbf{U}_I \\ \mathbf{U}_P \end{bmatrix} = \begin{bmatrix} \mathbf{0}_D \\ \mathbf{0}_I \\ \mathbf{0}_P \end{bmatrix} \tag{4}$$

Here, the subscripts D, I, P corresponds to the sampling points in the discrete homogeneous domains, the sampling points at the inner interfaces of the unit cell and the sampling points at the outer interface of the unit cell, respectively. $\lambda = e^{\mathrm{i}kL}$ represents the periodic boundary condition of the system. Detailed derivations can be found in Cheng et al. (2018).

Rearranging Eq. (4), one can obtain

$$\mathbb{F}(\omega,\lambda) = \det[\mathbf{\Phi}_{PP}(\lambda) - \mathbf{\Phi}_{PE}(\lambda)\mathbf{\Phi}_{EE}^{-1}(\omega)\mathbf{\Phi}_{EP}] = 0 \tag{5}$$

in which

$$\mathbf{\Phi}_{EE}(\omega) = \begin{bmatrix} \mathbf{\Phi}_{DD} - \omega^2 M_D & \mathbf{\Phi}_{DI} \\ \mathbf{\Phi}_{ID} & \mathbf{\Phi}_{II} \end{bmatrix}; \quad \mathbf{\Phi}_{EP} = \begin{bmatrix} \mathbf{\Phi}_{DP} \\ \mathbf{\Phi}_{IP} \end{bmatrix};$$

$$\mathbf{\Phi}_{PE}(\lambda) = \begin{bmatrix} \mathbf{\Phi}_{PD}(\lambda) \\ \mathbf{\Phi}_{PI}(\lambda) \end{bmatrix}^T$$

For given ω, four roots λ_n $(n = 1,2,3,4)$ can be obtained by solving Eq. (5). Then λ_n can be used to calculate k_n through

$$k_n = -1\mathrm{i} \times \log \lambda_n \tag{6}$$

which will give the complex dispersion relations.

2.3. Computational challenges

As shown in the previous section, to establish the complex dispersion relations for a given periodic structure, we need to solve Eq. (5) repeatedly for all the interested ω values. For example, to establish the complex dispersion relations shown in Fig. 1(c), which considers frequency in the range of [0, 2000] Hz with a frequency

interval/resolution of 0.1 Hz (i.e., 20001 frequencies and Eq. (5) needs to be solved 20001 times), using EDQEM, it takes around 1500 s (t_2) in total. In comparison, when using the DQEM, the real wave number varies in the first Brillouin zone $[-1, 1]$ with an interval of 0.01, and the wave numbers to be considered is 201. The total time is $t_1 = 0.3$ s, i.e., approximately 0.02% of t_2. Also, for the complex dispersion relations, when the number of frequencies increases, the computational effort will increase accordingly. Note that here the computational time for EDQEM is reported, and when more expensive numerical models (e.g., detailed finite element models) are used, the computational effort could be even higher. The computational effort could also increase with the dimension of the problem (e.g., more expensive when considering two-dimensional or three-dimensional periodic structures). Therefore, calculation of the detailed complex dispersion relations at large number of frequencies with fine frequency resolutions (e.g., tens of thousands of frequencies), which requires repeated solution of Eq. (5), could potentially entail significant computational effort.

Also, note that the example discussed above is for a specific periodic structure with specific material and geometrical properties. Many cases we need to repeatedly predict the complex dispersion relations for periodic structures with different properties. One example is uncertainty quantification. In practice there are various uncertainties related to the physical and geometrical properties. To investigate the impacts of these uncertainties on the dispersion relations and the resultant bandgap characteristics, we need to propagate these uncertainties. Fig. 1(d) shows the mean prediction of the complex dispersion relations and associated variability/uncertainty due to uncertainties in the properties of the considered periodic beam. Typically, stochastic simulation techniques (such as MCS) can be used. However, they typically requires large number of model evaluations. Therefore, direct calculation of the complex dispersion relations in the context of using stochastic simulation for uncertainty propagation entails huge computational effort. To facilitate the above tasks, efficient models are needed to predict the complex dispersion relations for periodic structures with different properties.

3. Adaptive Gaussian process model with PCA for prediction of complex dispersion relations

To address the above computational challenges, we propose an adaptive Gaussian process surrogate model to efficiently predict the complex dispersion relations at fine frequency resolution for periodic beams with different properties. The proposed approach is named AGP-PCA and is discussed in detail in this section.

3.1. Proper selection of inputs and outputs for Gaussian process model

For any given periodic beam characterized by input $\mathbf{x} = [x_1, \dots, x_i, \dots, x_{n_x}]$ of dimension n_x (including material and/or geometrical properties), our goal is to build GP model to predict the corresponding complex dispersion relations, or more specifically, calculate the corresponding $k_n = k_{\alpha,n} + \mathrm{i}k_{\beta,n}$ $(n = 1, 2, 3, 4)$ at specified frequencies denoted $\boldsymbol{\omega} = [\omega_1, \dots, \omega_i, \dots, \omega_{n_\omega}]$ where n_ω is the number of considered frequencies and $\omega_i \in [\omega_{lb}, \omega_{ub}]$ with ω_{lb} and ω_{ub} corresponding to the lower and upper bounds of the interested frequency range. Typically n_ω is a large number. The finer the frequency resolution, the larger n_ω is.

The direct way of formulating this problem might be to train GP model with $\mathbf{x}$ as input and $k_{\alpha,n}$ and $k_{\beta,n}$ at specified frequencies $\boldsymbol{\omega}$ as outputs. Let $\mathbf{y} = \mathbf{y}(\mathbf{x})$ represent the outputs, then we have $\mathbf{y}(\mathbf{x}) = [\mathbf{k}_{\alpha,n}(\mathbf{x}), \mathbf{k}_{\beta,n}(\mathbf{x})]$ where $\mathbf{k}_{\alpha,n} = [k_{\alpha,n}(\mathbf{x}, \omega_1), \dots, k_{\alpha,n}(\mathbf{x}, \omega_i), \dots, k_{\alpha,n}(\mathbf{x}, \omega_{n_\omega})]$ and $\mathbf{k}_{\beta,n} = [k_{\beta,n}(\mathbf{x}, \omega_1), \dots, k_{\beta,n}(\mathbf{x}, \omega_i), \dots, k_{\beta,n}(\mathbf{x}, \omega_{n_\omega})]$. In more general form, the outputs can be written as $\mathbf{y}(\mathbf{x}) = [y_1(\mathbf{x}), \dots, y_k(\mathbf{x}), \dots, y_{n_y}(\mathbf{x})]$ where n_y is the total number of outputs for given $\mathbf{x}$ and here $n_y = 8n_\omega$. Obviously, the outputs correspond to high-dimensional outputs.

Alternatively, we can treat λ_n (or more specifically, the real and imaginary parts of λ_n) as outputs. In this case, the output dimension is still $n_y = 8n_\omega$. However, for either taking k_n or λ_n as outputs for the GP model, the challenge is that the relationship $\mathbf{x} \rightarrow \mathbf{y}(\mathbf{x})$ might be non-smooth. This is especially the case when there is no damping considered in the system. Mathematically, the reasons for this are: (i) the roots λ_n (or more specifically, the real and imaginary parts of λ_n) are non-smooth functions of $\mathbf{x}$, and (ii) when k_n is the output, the transformation $k_n = -1\mathrm{i} \times \log \lambda_n$ means that the real and imaginary parts of k_n also have non-smooth variation with respect to $\mathbf{x}$. Therefore, directly training GP model with either k_n or λ_n as outputs has challenges in certain regions of $\mathbf{x}$ where the functional relationship $\mathbf{x} \rightarrow \mathbf{y}(\mathbf{x})$ is non-smooth, which will reduce the accuracy of the trained GP model. The low accuracy in predicting where the non-smoothness happens has important implications in the current problem since the location determines or corresponds to where the bandgap starts or ends.

To address the non-smoothness here, we reformulate the problem as follows. Here instead of directly training GP model with k_n or λ_n as outputs, we train GP model for the coefficients of the quartic equation in Eq. (5), which are continuous and smooth functions of $\mathbf{x}$. Once the coefficients are established, they are then plugged into the analytical solutions of the quartic equation to find the corresponding λ_n $(n = 1, \cdots, 4)$, which can be further plugged into Eq. (6) to calculate the corresponding k_n $(n = 1, \cdots, 4)$.

First, for given $\mathbf{x}$ and ω, the quartic equation with respect to λ is written explicitly as

$$c_1(\mathbf{x}, \omega)\lambda^4 + c_2(\mathbf{x}, \omega)\lambda^3 + c_3(\mathbf{x}, \omega)\lambda^2 + c_4(\mathbf{x}, \omega)\lambda + c_5(\mathbf{x}, \omega) = 0 \tag{7}$$

In the current problem, we found that $c_1(\mathbf{x}, \omega) = c_5(\mathbf{x}, \omega)$ and $c_2(\mathbf{x}, \omega) = c_4(\mathbf{x}, \omega)$. Further normalizing the equation by $c_1(\mathbf{x}, \omega)$ leads to an equivalent equation with two unique coefficients $\xi_1(\mathbf{x}, \omega)$ and $\xi_2(\mathbf{x}, \omega)$,

$$\lambda^4 + \xi_1(\mathbf{x}, \omega)\lambda^3 + \xi_2(\mathbf{x}, \omega)\lambda^2 + \xi_1(\mathbf{x}, \omega)\lambda + 1 = 0 \tag{8}$$

where $\xi_1(\mathbf{x}, \omega) = c_2(\mathbf{x}, \omega)/c_1(\mathbf{x}, \omega)$ and $\xi_2(\mathbf{x}, \omega) = c_3(\mathbf{x}, \omega)/c_1(\mathbf{x}, \omega)$. Note that $\xi_1(\mathbf{x}, \omega)$ and $\xi_2(\mathbf{x}, \omega)$ are real numbers when there is no damping, and they become complex numbers when damping is considered.

As an illustration, we consider the case of $\mathbf{x}$ being a scalar x. Fig. 2 shows the variation of $k_{\alpha,n}(x, \omega)$ and $k_{\beta,n}(x, \omega)$ $(n = 1, \cdots, 4)$ as a function of x under a selected ω value for the case when no damping is considered. The "kinks" in the functions can be clearly seen; for $k_{\alpha,1}$ and $k_{\alpha,2}$ there is no variation before the "kinks" as x varies, while for $k_{\beta,1}$ and $k_{\beta,2}$ there is no variation after the "kinks" as x varies. Fig. 3 shows the corresponding variation of $\xi_1(x, \omega)$ and $\xi_2(x, \omega)$ as a function of x. As can be seen, $\xi_1(x, \omega)$ and $\xi_2(x, \omega)$ are continuous and smooth functions of x.

Similarly, Fig. 4 shows the variation of $k_{\alpha,n}(x, \omega)$ and $k_{\beta,n}(x, \omega)$ $(n = 1, \cdots, 4)$ as a function of x under a selected ω value for the case when damping is considered. In this case, because of the damping, the "kinks" that were present for the case with no damping were not there anymore and the functions become smooth. In this sense, the prediction of complex band structure for cases with damping is less challenging than cases without damping. However, from part (a) of the figure, it can be seen that still for most of the range of x considered here the variation of $k_{\alpha,1}$ and $k_{\alpha,2}$ is quite small (almost stay constant), while after around $x = 1.15$, the variation becomes more obvious. This type of function will still create some challenges in building surrogate model. Fig. 5 shows the corresponding variation of the real and imaginary parts of $\xi_1(x, \omega)$ and $\xi_2(x, \omega)$ as a function of x. As can be seen, both the real and imaginary parts of $\xi_1(x, \omega)$ and $\xi_2(x, \omega)$ are continuous and smooth functions of x with much obvious trend/variation information, which makes training surrogate models for them easier.

Therefore, we will build GP model for the coefficients ξ_1 and ξ_2. The outputs then correspond to $\mathbf{y}(\mathbf{x}) = [\xi_1(\mathbf{x}, \omega_1), \dots, \xi_1(\mathbf{x}, \omega_i), \dots, \xi_1(\mathbf{x}, \omega_{n_\omega}), \xi_2(\mathbf{x}, \omega_1), \dots, \xi_2(\mathbf{x}, \omega_i), \dots, \xi_2(\mathbf{x}, \omega_{n_\omega})]$ with dimension $n_y = 2n_\omega$ when there is no damping. When damping is considered, the outputs then correspond to real $(\Re)$ and imaginary $(\Im)$ parts of the coefficients,

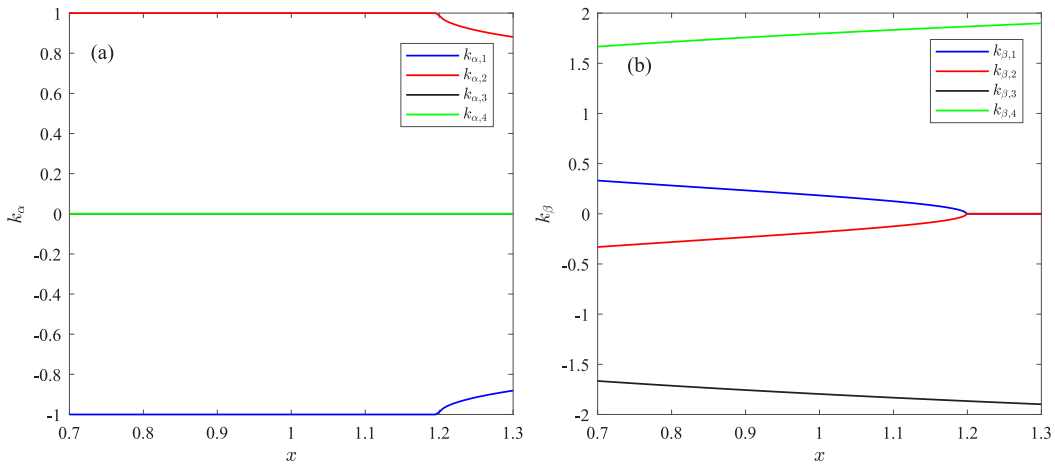

Fig. 2. Variation of (a) $k_{\alpha,n}(x,\omega)$ and (b) $k_{\beta,n}(x,\omega)$ as a function of x under selected ω.

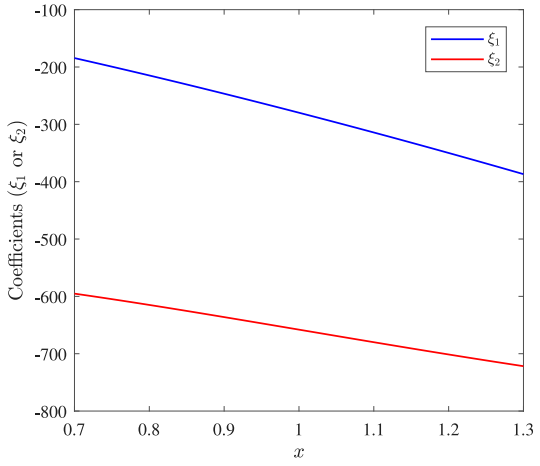

Fig. 3. Variation of $\xi_1(x,\omega)$ and $\xi_2(x,\omega)$ as a function of x under selected ω.

i.e., $\mathbf{y}(\mathbf{x}) = [\Re(\xi_1(\mathbf{x},\omega_1)), \Im(\xi_1(\mathbf{x},\omega_1)), \ldots, \Re(\xi_1(\mathbf{x},\omega_i)), \Im(\xi_1(\mathbf{x},\omega_i)), \ldots, \Re(\xi_1(\mathbf{x},\omega_{n_\omega})), \Im(\xi_1(\mathbf{x},\omega_{n_\omega})), \Re(\xi_2(\mathbf{x},\omega_1)), \Im(\xi_2(\mathbf{x},\omega_1)), \ldots, \Re(\xi_2(\mathbf{x},\omega_i)), \Im(\xi_2(\mathbf{x},\omega_i)), \ldots, \Re(\xi_2(\mathbf{x},\omega_{n_\omega})), \Im(\xi_2(\mathbf{x},\omega_{n_\omega}))]$ with dimension $n_y = 4n_\omega$.

Note that based on Eq. (8) we know that the coefficients ξ_1 and ξ_2 are functions of both $\mathbf{x}$ and ω. Intuitively, we should be able to build surrogate model with both $\mathbf{x}$ and ω as inputs, and then use surrogate model to directly predict the coefficients ξ_1 and ξ_2 for not only different $\mathbf{x}$ values but also different ω values. This will eliminate the need to consider high-dimensional outputs as well. However, through our investigation it was found that the coefficients are in general more sensitive to the variation in $\mathbf{x}$ than ω, if training GP model with both of them as inputs, the variation of the coefficients due to variation in ω will be difficult to capture, especially when $\mathbf{x}$ varies in a large range. This will lead to larger error and lower accuracy of the established GP model. More importantly, since many times we are interested in accurately predicting the complex dispersion relations (defined by frequencies and corresponding λ_n pairs) under different $\mathbf{x}$, it is desirable to treat $\mathbf{x}$ as inputs and treat the corresponding entire complex dispersion relations as outputs. Therefore, to improve the prediction accuracy for the complex dispersion relations, we train GP model with $\mathbf{x}$ as inputs and with $\mathbf{y}(\mathbf{x}) = [\xi_1(\mathbf{x},\omega_1), \ldots, \xi_1(\mathbf{x},\omega_i), \ldots, \xi_1(\mathbf{x},\omega_{n_\omega}), \xi_2(\mathbf{x},\omega_1), \ldots, \xi_2(\mathbf{x},\omega_i), \ldots, \xi_2(\mathbf{x},\omega_{n_\omega})]$ as outputs.

To build the GP model, we first run n_{lhs} evaluations of the numerical model (e.g., EDQEM for the current problem) and establish a database, which consists of an output vector $\{\mathbf{y}^h = \mathbf{y}(\mathbf{x}^h); h = 1, \ldots, n_{lhs}\}$ for each input $\{\mathbf{x}^h; h = 1, \ldots, n_{lhs}\}$. The database $\{\mathbf{x}^h, \mathbf{y}(\mathbf{x}^h); h = 1, \ldots, n_{lhs}\}$ is frequently referenced as the *training set*. The selection of input $\{\mathbf{x}^h; h = 1, \ldots, n_{lhs}\}$ will impact the accuracy of the GP model. Initially, to ensure the model have good prediction accuracy over the entire input space, selections that can evenly fill the input space is typically used. For this purpose, Latin Hypercube Sampling (LHS) is used here. We will denote by $\mathbf{X} = [\mathbf{x}^1, \ldots, \mathbf{x}^{n_{lhs}}]^T \in \mathbb{R}^{n_{lhs} \times n_x}$ and $\mathbf{Y} = [\mathbf{y}^1, \ldots, \mathbf{y}^{n_{lhs}}]^T \in \mathbb{R}^{n_{lhs} \times n_y}$ the corresponding input and output matrices, respectively. Later an adaptive sampling procedure is introduced to sequentially add training data that most effectively improve the accuracy of the built GP model. The integration of the adaptive procedure is another novel component of the proposed approach.

3.2. Gaussian process model with PCA

To address the challenge of building surrogate model for high-dimensional outputs (i.e., n_y is large), the kriging with PCA approach proposed in Jia and Taflanidis (2013) and Jia et al. (2016) is adopted. The overall idea is to use PCA to first reduce the dimensionality of the outputs, then surrogate model is efficiently built with respect to the low-dimensional latent outputs. For prediction at new inputs, first, the corresponding latent outputs are predicted, which are then directly transformed back to the high-dimensional outputs through the inverse PCA transformation. One benefit of using PCA is that it can automatically capture the correlation between the outputs. For the current problem, that means the correlation between ξ_1 and ξ_2 as well as between their values at different frequencies can be automatically captured, which helps improve the prediction accuracy of the roots and the complex dispersion relations.

3.2.1. Output dimension reduction by PCA

PCA is used to reduce the dimension of the outputs corresponding to coefficients at selected frequencies. The corresponding low-dimensional outputs are established by considering the eigenvalue problem for the covariance matrix $\Sigma^{\mathbf{y}} = \mathbf{Y}^T\mathbf{Y}$, and only the latent outputs and associated eigenvectors corresponding to the n_z largest eigenvalues are retained (Jolliffe, 2011). The latent output matrix of size $n_{lhs} \times n_z$, which is needed for developing surrogate models in latent space, can be established through the transformation

$$\mathbf{Y}^T = \mathbf{P}\mathbf{Z}^T, \tag{9}$$

where $\mathbf{P}$ is the $n_y \times n_z$ projection matrix containing the eigenvectors corresponding to the n_z largest eigenvalues. The value of n_z can be chosen so that $r_c \geq r_o$, where r_c is the proportion of the total variance of original outputs accounted by the largest n_z eigenvalues and r_o is a threshold value (e.g., $r_o = 99.99\%$). This leads to latent outputs accounting for at least r_o of the total variance of the data in $\mathbf{Y}$ (Tipping

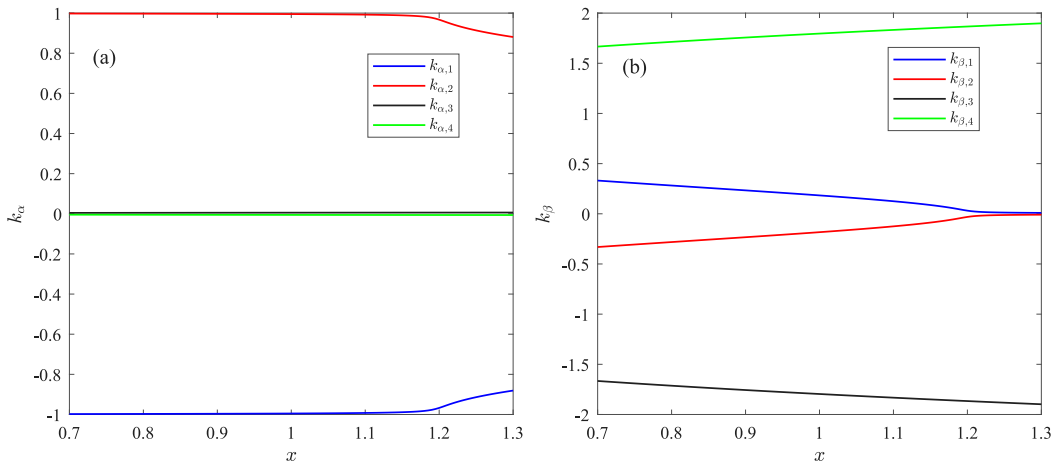

Fig. 4. Variation of (a) $k_{\alpha,n}(x,\omega)$ and (b) $k_{\beta,n}(x,\omega)$ as a function of x under selected ω for the case that considers damping.

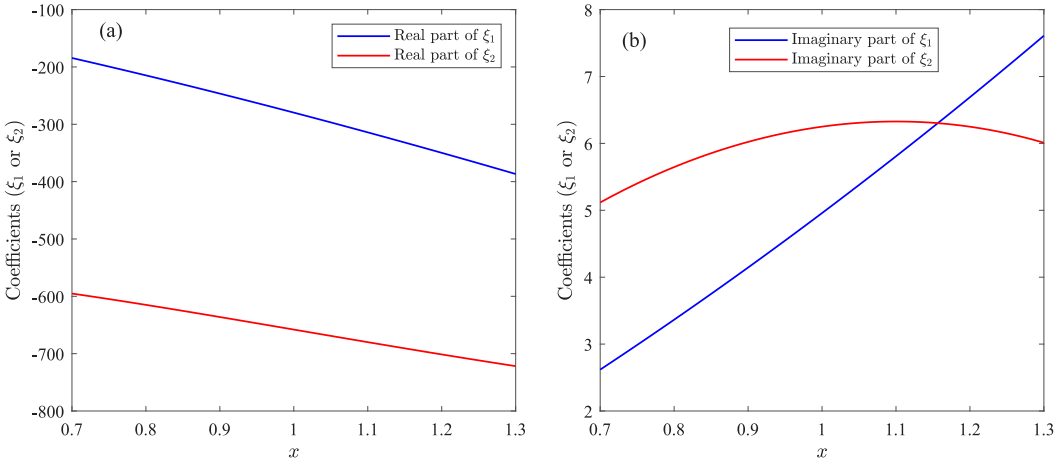

Fig. 5. Variation of $\xi_1(x,\omega)$ and $\xi_2(x,\omega)$ as a function of x under selected ω for the case that considers damping. (a) shows the real part of ξ_1 and ξ_2, and (b) shows the imaginary part of ξ_1 and ξ_2.

and Bishop, 1999). More specifically, if λ_j is the jth largest eigenvalue, then this selection is facilitated by selecting n_z so that the ratio $r_c = \sum_{j=1}^{n_z}\lambda_j / \sum_{j=1}^{n_y}\lambda_j$ is greater than r_o. Typically, $n_z \ll n_y$, leading to a significant reduction in the output dimension. With the latent output matrix $\mathbf{Z}$ established through the transformation in Eq. (9), GP model can be developed for the low-dimensional latent outputs.

3.2.2. Gaussian process surrogate model for latent outputs

The set $\{\mathbf{X},\mathbf{Z}\}$ (i.e., $\{\mathbf{x}^h, \mathbf{z}(\mathbf{x}^h); h = 1,\dots,n_{lhs}\}$) then forms a training set for surrogate modeling. GP model is then built based on the training set and used to predict the latent outputs at new inputs instead of running the original numerical model. Due to the low dimensionality of the latent outputs $\mathbf{z}$, a single surrogate model can be built with respect to each or all of the latent outputs in $\mathbf{z}$ (Jia and Taflanidis, 2013; Jia et al., 2016). Here a single GP model is built for $\mathbf{z}$. Based on the training data, GP model establishes an approximation/prediction to $\mathbf{z}(\mathbf{x})$, denoted $\hat{\mathbf{z}}(\mathbf{x})$, for any new input $\mathbf{x}$ through (Sacks et al., 1989)

$$\hat{\mathbf{z}}(\mathbf{x}) = \mathbf{f}(\mathbf{x})^T\boldsymbol{\alpha}^* + \mathbf{r}(\mathbf{x})^T\boldsymbol{\beta}^*, \tag{10}$$

where $\mathbf{f}(\mathbf{x})$ is the n_p-dimensional basis vector (e.g., linear or quadratic polynomials of $\mathbf{x}$), $\boldsymbol{\alpha}^* = (\mathbf{F}^T\mathbf{R}^{-1}\mathbf{F})^{-1}\mathbf{F}^T\mathbf{R}^{-1}\mathbf{Z}$ and $\boldsymbol{\beta}^* = \mathbf{R}^{-1}(\mathbf{Z}-\mathbf{F}\boldsymbol{\alpha}^*)$ are $n_p \times n_z$ and $n_{lhs}\times n_z$ dimensional coefficient matrices, and $\mathbf{F} = [\mathbf{f}(\mathbf{x}^1)\dots\mathbf{f}(\mathbf{x}^{n_{lhs}})]^T$ is the $n_{lhs}\times n_p$ basis matrix. For the linear and quadratic cases, n_p equals to (n_x+1) and $(n_x+1)(n_x+2)/2$, respectively. $\mathbf{R}$ is the $n_{lhs}\times n_{lhs}$ correlation matrix with the jk^{th} element defined as the correlation function $R(\mathbf{x}^j,\mathbf{x}^k)$. One commonly used correlation function is the generalized exponential correlation with tuning parameters $\mathbf{s} = [s_1,\dots,s_{n_x+1}]$,

$$R(\mathbf{x}^j,\mathbf{x}^k) = \prod_{i=1}^{n_x}\exp\left[-s_i|x_i^j - x_i^k|^{s_{n_x+1}}\right]. \tag{11}$$

$\mathbf{r}(\mathbf{x})$ is the $n_{lhs}-$dimensional correlation vector $\mathbf{r}(\mathbf{x}) = [R(\mathbf{x},\mathbf{x}^1),\dots, R(\mathbf{x},\mathbf{x}^{n_{lhs}})]^T$ between the new input $\mathbf{x}$ and each of the elements of $\mathbf{X}$. Through the proper tuning of the parameters $\mathbf{s}$ in the correlation function, GP model can efficiently approximate very complex functions. The optimal selection of $\mathbf{s}$ is typically based on the Maximum Likelihood Estimation (MLE) principle, and standard approaches for solving this optimization are given in Lophaven et al. (2002). Besides the predictor in Eq. (10), GP model also provides the local variance of the predictor. This variance is a local estimate, meaning that it is a function of the input $\mathbf{x}$ and not constant over the entire input domain. This local variance information about the GP prediction can be explicitly incorporated if needed.

3.2.3. Prediction for the original high-dimensional outputs

For prediction at new input $\mathbf{x}$, first the GP model predicts the corresponding latent outputs. Based on the predictor for the latent outputs, the predictor for the original high-dimensional outputs $\mathbf{y}(\mathbf{x})$ is established using the linear transformation

$$\hat{\mathbf{y}}(\mathbf{x})^T = \mathbf{P}\hat{\mathbf{z}}(\mathbf{x})^T \tag{12}$$

where $\hat{\mathbf{z}}(\mathbf{x}) = [\hat{z}_1(\mathbf{x}),\dots,\hat{z}_l(\mathbf{x}),\dots,\hat{z}_{n_z}(\mathbf{x})]$.

3.3. Adaptive GP with PCA

To reduce the number of training data required to reach targeted level of accuracy for the GP model, here we employ an adaptive sampling procedure to sequentially add training data that most effectively improve the accuracy of the GP model and the predicted complex dispersion relations. A key step of the adaptive sampling is to choose an appropriate infill criterion to balance the local exploitation as well as the global exploration for the selection of new samples in each iteration. Weighted accumulative error (WAE), defined based on the weighted leave-one-out cross validation (LOOCV) prediction error (Jiang et al., 2015), is adopted in this paper. The infill criterion $e(\mathbf{x})$ is expressed by

$$e(\mathbf{x}) = \sqrt{\sum_{i=1}^{n_t} w_i(\mathbf{x})(\hat{y}(\mathbf{x}) - \hat{y}_{-i}(\mathbf{x}))^2} \tag{13}$$

where $\hat{y}(\mathbf{x})$ is the prediction at $\mathbf{x}$ from the GP model built on all n_t training data, $\hat{y}_{-i}(\mathbf{x})$ is the prediction at $\mathbf{x}$ from the GP model built on the training data except the ith data $\mathbf{x}^i$, and $w_i(\mathbf{x})$ is the weight at $\mathbf{x}$ for the corresponding prediction error, given by $w_i(\mathbf{x}) = \exp(-\|\mathbf{x} - \mathbf{x}^i\|)/\sum_{j=1}^{n_t}\exp(-\|\mathbf{x} - \mathbf{x}^j\|)$. Note that Eq. (13) is used to calculate WAE for scalar response $\hat{y}(\mathbf{x})$, and if the response is multi-dimensional, the squared error $(\hat{y}(\mathbf{x}) - \hat{y}_{-i}(\mathbf{x}))^2$ in the equation can be substituted by the mean squared error (i.e., averaging squared errors over all the dimensions), which is used in this paper.

By solving the optimization problem (i.e., maximizing $e(\mathbf{x})$), one or multiple new sample points can be selected and added to the existing training set. It is noteworthy to point out that in order to avoid clustered new samples, a minimum distance constraint between the new samples and the existing samples is introduced for the optimization. To implement the adaptive sampling, we first generate n_{lhs} (a small number) training data, and evaluate the EDQEM method to obtain the corresponding response. The GP model is initially trained based on this data. Then the new sample $\mathbf{x}_{add}$ that maximizes the WAE, calculated according to Eq. (13), is found by running an optimization. Since calculation of the objective function $e(\mathbf{x})$ in Eq. (13) only involves prediction from GP models, the overall optimization is quite efficient. The new sample is then added to the training set, and the corresponding response of the sample is calculated with the EDQEM method. Finally, the GP model is updated with the new training set. This adaptive addition of new sample points can be carried out iteratively until some convergence criterion is reached, e.g., setting an upper limit on the number of iterations, or a target level for the model prediction accuracy.

3.4. Accuracy assessment

To assess the accuracy of the AGP model, LOOCV is used to estimate the error statistics over the training set. Commonly used error statistics include coefficient of determination (R^2) and mean squared error (MSE), which are applied here. These statistics can be established for both the latent outputs and the original outputs. For the kth output, the corresponding R_k^2 and MSE_k are defined as

$$R_k^2 = 1 - \frac{\sum_{h=1}^{n_t}(y_k^h - \hat{y}_k^h)^2}{\sum_{h=1}^{n_t}(y_k^h - \bar{y}_k)^2}; \quad MSE_k = \frac{\sum_{h=1}^{n_t}(y_k^h - \hat{y}_k^h)^2}{n_t} \tag{14}$$

where n_t is the number of training data, y_k^h is the actual response over the hth input, $\hat{y}_k^h$ is the predicted value of y_k^h, and $\bar{y}_k$ is the mean of y_k^h over all the training data. Larger values for R_k^2 (close to one) and smaller values for MSE_k (closer to zero) indicate better accuracy of the surrogate model. Further, the average R^2 and MSE over all output dimensions can be established by $\sum_{k=1}^{n_y} R_k^2/n_y$ and $\sum_{k=1}^{n_y} MSE_k/n_y$, respectively, which can be used to assess the overall accuracy of the surrogate model in predicting the multi-dimensional outputs.

3.5. AGP-PCA based prediction of complex dispersion relations

For prediction at new input $\mathbf{x}$, the trained adaptive GP model with PCA will be used to predict the coefficients for the quartic equation. Then the coefficients are plugged into the analytical solutions of the quartic equation to find the corresponding λ_n, which can be plugged into Eq. (6) to calculate k_n and establish the complex dispersion relations. The flowchart for the proposed AGP-PCA approach to predict complex dispersion relations for periodic structures is shown in Fig. 6, which shows the key steps. Note that in the flowchart the output dimension n_y is shown for the case when there is no damping, i.e., $n_y = 2n_\omega$. When damping is considered, the outputs would include both the real ($\Re$) and imaginary ($\Im$) parts of the coefficients, in which case the output dimension $n_y = 4n_\omega$.

4. Illustrative example

To illustrate the correctness and better performance of the proposed approach, we consider the prediction of the complex dispersion relations of periodic concrete–steel beams.

4.1. Implementation details

In terms of material properties, for steel, it has elastic modulus of $E_{st} = 210$ GPa, shear modulus of $G_{st} = 78.95$ GPa, and density of $\rho_{st} = 7850$ kg/m^3; for concrete, it has elastic modulus of $E_{con} = 25$ GPa, shear modulus of $G_{con} = 9.40$ GPa, and density of $\rho_{con} = 2300$ kg/m^3. In terms of geometrical parameters, for the concrete segment, the cross section area $A_1 = 0.1$ m^2, with moment of inertia $I_1 = 2.083 \times 10^{-3}$ m^4, and length $L_1 = 1.0$ m. For the steel segment, the corresponding parameters are represented by A_2, I_2, and L_2. To investigate the impact of the relative geometrical properties on the dispersion relations, we vary the geometrical properties of the steel segment. For this purpose, we define $\mathbf{x} = [x_1, x_2, x_3]$ where $x_1 = A_2/A_1$, $x_2 = I_2/I_1$, and $x_3 = L_2/L_1$. The range of x_i is taken as [0.7, 1.3]. To establish the training data, EDQEM method is used. For EDQEM, the number of sampling points is taken as 12. The range of frequency is selected as 1 to 2000 Hz with frequency resolution of 1 Hz, leading to $n_{lhs,\omega} = 2000$ and $n_y = 4000$. For the investigation, in the first two subsections of Section 4.2 we first focus on the case without damping, which is the more challenging case, and later in Section 4.2.3 also show the results and comparisons for the case with damping.

4.2. Performance of the proposed AGP-PCA

4.2.1. Adaptive selection of the training data

The initial number of training data n_{lhs} is selected as 30, and then the adaptive procedure is used to sequentially add training data. To select an appropriate total number of the training data n_t, we investigate how the model accuracy changes over different n_t. The prediction accuracy of the AGP-PCA model is assessed by the R^2 and MSE calculated based on LOOCV. For the infill criterion WAE, first the WAE for ξ_1, ξ_2 (i.e., the high-dimensional outputs correspond to the ξ_1, ξ_2) is used as the infill criterion in the adaptive sampling. The trained AGP-PCA model is referred as AGP_{ξ_1,ξ_2}. In addition, we also trained another model where the adaptive sampling uses the WAE for k_α, k_β as the infill criterion. This model is referred as $\text{AGP}_{k_\alpha,k_\beta}$. Since the ultimate goal is to establish AGP-PCA model that can accurately predict the complex dispersion relations (i.e., k_α, k_β), we compare the accuracy of these two models by the error statistics calculated for k_α, k_β by these two models.

Fig. 7 shows the variation of the average R^2 and MSE for k_α, k_β against n_t for both models. As expected, the prediction accuracy for both models improve as n_t increases, especially at the beginning stage (i.e., small n_t). When n_t is larger than 120, there is little improvement in the model accuracy and high average R^2 values are established for

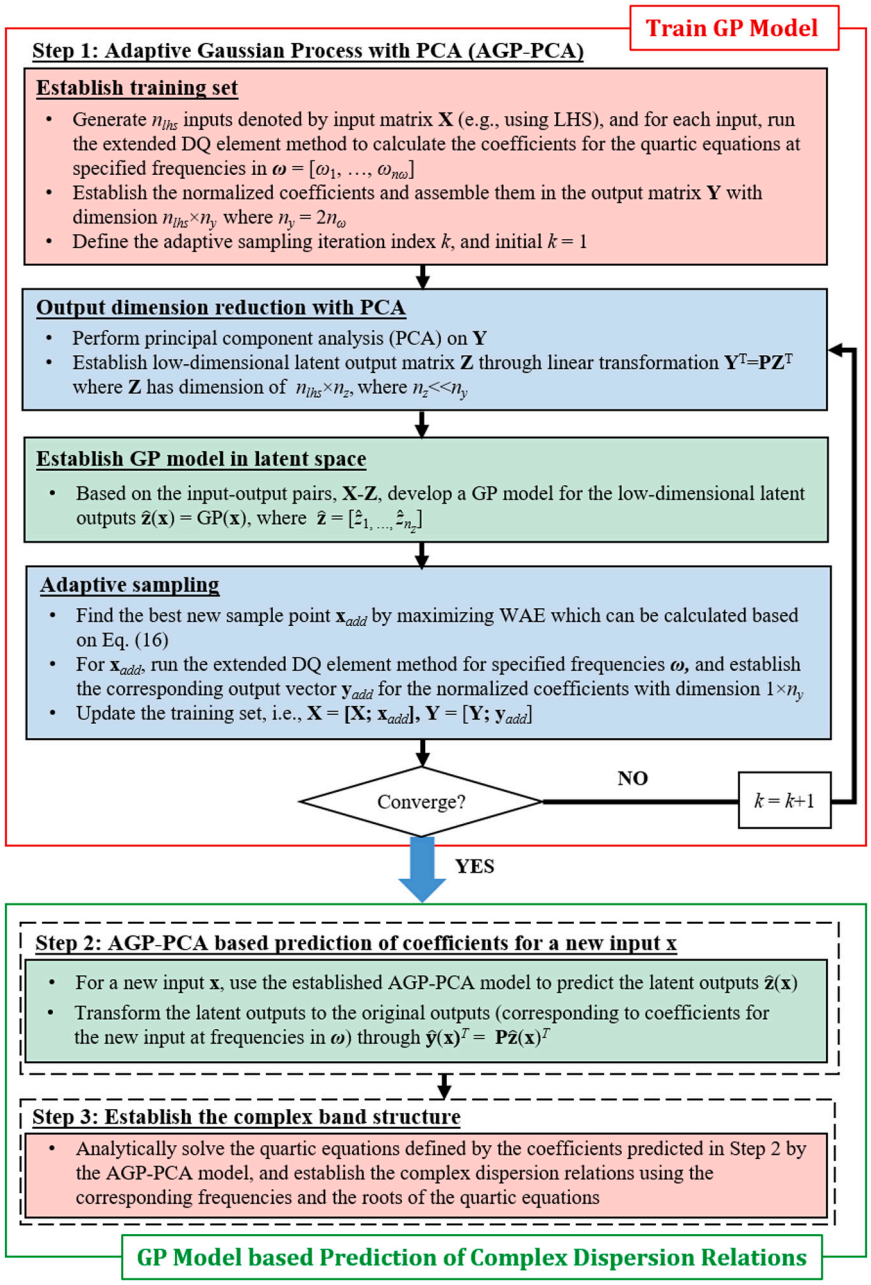

Fig. 6. Flowchart of the proposed AGP-PCA approach for prediction of complex dispersion relations for periodic structures.

both models. Comparing the two models, we can see that the model that uses WAE for k_α, k_β has better accuracy (albeit not by much in the current example). This better accuracy is attributed to the fact that the adaptive sampling tries to add sample points to best improve the accuracy in terms of k_α, k_β; on the other hand, the model that uses WAE for ξ_1, ξ_2 tries to add sample points to best improve the accuracy in terms of ξ_1, ξ_2. Although overall smaller error for ξ_1, ξ_2 would indicate smaller error for k_α, k_β as well, due to the complex relationship between ξ_1, ξ_2 and k_α, k_β, the samples that most effectively improve the accuracy in terms of ξ_1, ξ_2 may not necessarily be the same as those that most effectively improve the accuracy in terms of k_α, k_β. For example, it was found that for some ξ_1, ξ_2 values, even if there are relatively large errors, such errors only have small impact on the k_α, k_β values (i.e., only lead to small errors in the predicted k_α, k_β). While for some ξ_1, ξ_2 values, small errors may lead to large error in the predicted k_α, k_β and complex dispersion relations. Overall, the comparison shows that using WAE for k_α, k_β as infill criterion for the adaptive sampling should be preferred, which is used for the rest of the investigations in this paper.

Fig. 8 shows the samples added over the iterations for the adaptive sampling using WAE for k_α, k_β as infill criterion, including histograms of samples for x_1, x_2, and x_3 as well as the two dimensional plots of the samples. The circles correspond to the initial 30 samples, while the solid circles correspond to the added samples. As can be seen, for all three inputs (especially x_1, x_2), more samples are added close to some of the boundary regions where the combinations of x_1, x_2, and x_3 could lead to large magnitude/variations in the ξ_1, ξ_2 values, which may lead to potentially large prediction errors for ξ_1, ξ_2 values and the corresponding k_α, k_β values.

In the end, $n_t = 150$ training data is used. PCA is applied to the outputs of the training data, and it was found that only $n_z = 15$ latent outputs are needed to represent the original $n_y = 4000$ outputs (i.e., capturing more than 99.999% of the total variance in the output data), corresponding to large reduction in the output dimension. The

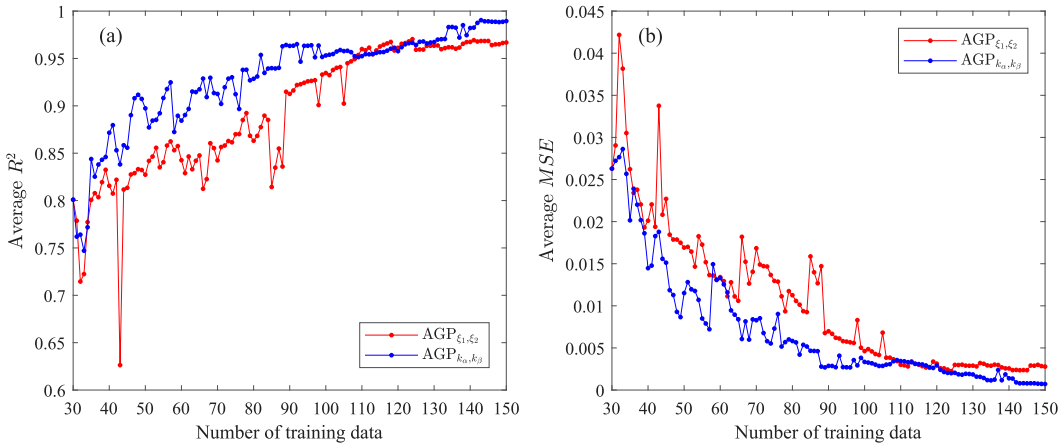

Fig. 7. Variation of (a) the average R^2 and (b) MSE for k_α, k_β against the number of training data for two AGP models, where one model is trained using WAE for ξ_1, ξ_2 for the adaptive sampling, while the other uses WAE for k_α, k_β for the adaptive sampling.

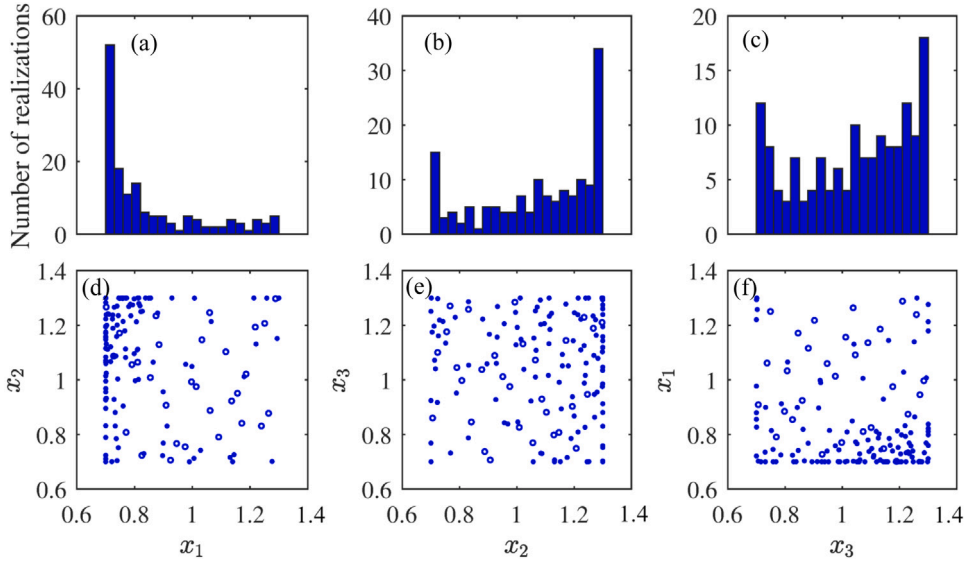

Fig. 8. Histogram of samples of (a) x_1, (b) x_2 and (c) x_3, and the samples added over the iterations for the adaptive sampling using WAE for k_α, k_β as infill criterion, shown for (d) [x_1, x_2], (e) [x_2, x_3], and (f) [x_3, x_1] where the open circles correspond to the initial 30 samples, while the solid circles correspond to the added samples.

variation of the captured variance against the number of principal components used is shown in Fig. 9.

4.2.2. Accuracy of the AGP model

To illustrate the performance of the GP model, it is applied to predict the complex dispersion relation for given **x**. First the accuracy in the predicted coefficients will be discussed, and then the predicted complex dispersion relation will be compared with those from EDQEM. Fig. 10 shows the $\xi_1(\omega)$ and $\xi_2(\omega)$ predicted by EDQEM and AGP-PCA at $\boldsymbol{\omega}$ for $\mathbf{x} = [1, 1, 1]$. In the figure, close match (almost overlap) between EDQEM and AGP-PCA can be observed. Fig. 11 compares the corresponding complex dispersion relations obtained by EDQEM and AGP-PCA for $\mathbf{x} = [1, 1, 1]$. At a glance, these two dispersion structures are identical. Further, detailed comparisons of dispersion relations of different wave modes are shown in Fig. 12. Obviously, the prediction of dispersion relations of different wave modes by AGP-PCA closely matches the prediction by EDQEM.

Once the complex dispersion relations are predicted, then the corresponding bandgap characteristics can be extracted, which are important information for design and application purpose. This way of first predicting the complex dispersion relations and then extracting the corresponding bandgap characteristics are attractive considering the

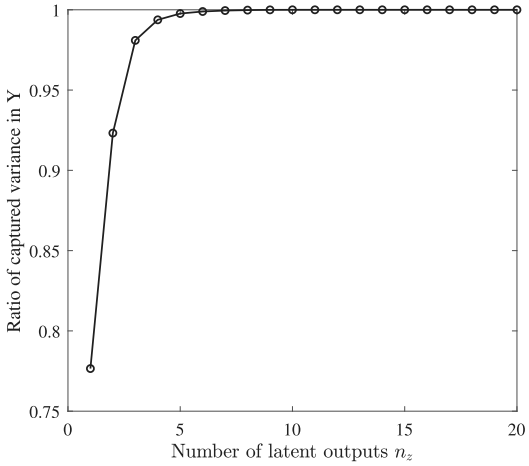

Fig. 9. Variation of the captured variance against the number of latent outputs used.

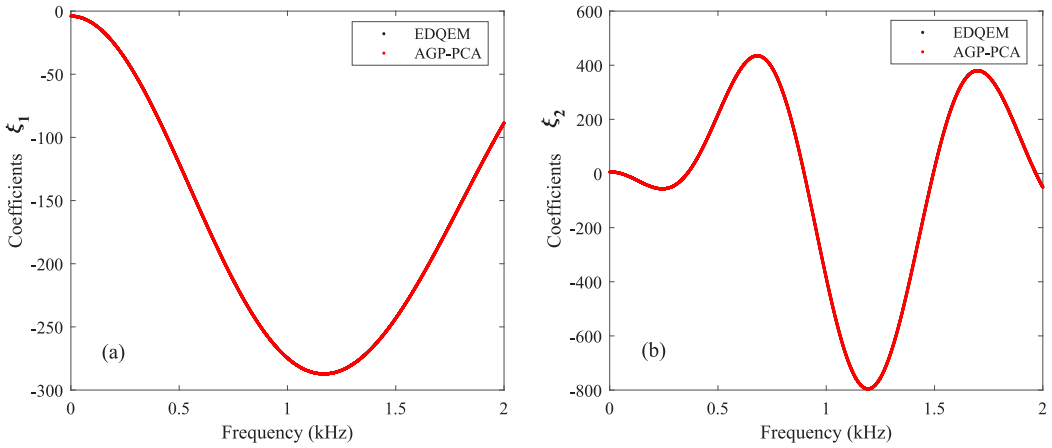

Fig. 10. (a) $\xi_1(\omega)$ and (b) $\xi_2(\omega)$ predicted by EDQEM and AGP-PCA for $\mathbf{x} = [1, 1, 1]$.

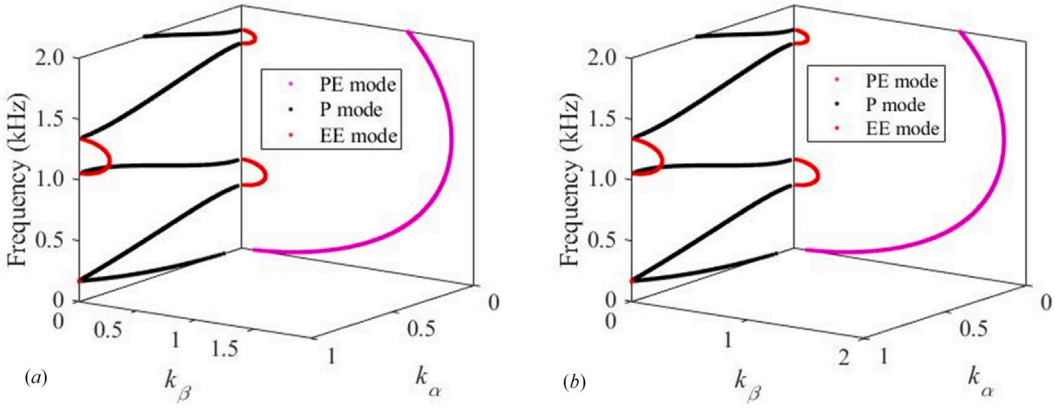

Fig. 11. Complex dispersion relations calculated by (a) EDQEM and (b) AGP-PCA for $\mathbf{x} = [1, 1, 1]$.

Table 1
Bandgap characteristics for $\mathbf{x} = [1, 1, 1]$ predicted by different numerical $k(\omega)$ methods.

Methods	First bandgap			Fourth bandgap			DOFs	N_L	Time (s)
	LBF	UBF	$max\|k_\beta^1\|$	LBF	UBF	$max\|k_\beta^4\|$			
WFEM (Mace and Manconi, 2008)	162.5	172.5	0.0139	1692.5	1812.5	0.3892	42	2000	1040
EDQEM (Cheng et al., 2018)	162.5	171.5	0.014	1684.5	1796.5	0.1178	40	2000	150
AGP-PCA	162.5	171.5	0.0138	1685.5	1796.5	0.1170	–	–	0.004

fact that directly predicting the bandgap characteristics is challenging (e.g., directly build surrogate model for the bandgap characteristics). This is because as $\mathbf{x}$ varies the bandgaps in a certain frequency range may exist for some $\mathbf{x}$ values, but may not exist for other $\mathbf{x}$ values, creating discontinuity and challenge for directly predicting the bandgap characteristics. Table 1 shows the bandgap characteristics extracted based on the corresponding complex dispersion relations predicted by EDQEM and AGP-PCA. The characteristics include LBF, UBF, and the maximum attenuation parameter for the nth bandgap (i.e., $\max|k_\beta^n|$) with $n = 1, \ldots, 4$, where LBF and UBF are the lower and upper bound frequencies of a bandgap, respectively. For validation and comparison purpose, results obtained by the WFEM (Mace and Manconi, 2008) are also given. It is clear that results obtained by the proposed AGP-PCA method match well with those obtained by both the EDQEM and the WFEM. More importantly, the computational time of the AGP-PCA method is much smaller than those of the other two numerical methods. The benefit of using the established GP model is that it can easily accommodate even finer resolutions without the need to run EDQEM numerical model.

4.2.3. Complex dispersion relations of damped systems

Complex dispersion relations of damped systems are also predicted by the proposed AGP-PCA method. Here, complex damping model is used to include the material viscosity, and the Young's modulus E is replaced by $\mathrm{E}' = \mathrm{E}(1+\mathrm{i}\eta)$ with η the material loss factor. For simplicity, the material damping of concrete is considered with the material loss factor $\eta = 0.015$, and the material damping of steel is neglected (Cheng et al., 2018).

Fig. 13 compares the complex dispersion relations of the damped periodic concrete–steel beam obtained by EDQEM and AGP-PCA. As expected, because of the material viscosity effect, all wave modes transfer into the damped complex waves. The sharp corners at the bound frequencies of bandgaps of the undamped system become rounded. And, no clear bandgap can be identified. On the other hand, since the non-smoothness of the dispersion relation curves is not present for the damped system, the challenge for the proposed AGP-PCA method in obtaining accurate prediction is also reduced. Good agreements between AGP-PCA and EDQEM can be observed in Fig. 13. Besides the great accuracy, the AGP-PCA maintains great efficiency and the computational time of AGP-PCA is much smaller than that of EDQEM.

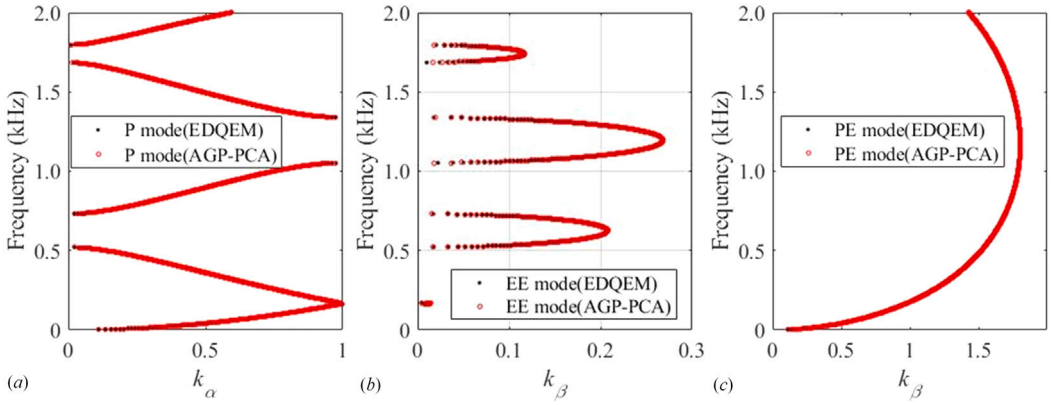

Fig. 12. (a) P mode, (b) EE mode and (c) PE mode dispersion structures predicted by EDQEM and by AGP-PCA for $\mathbf{x} = [1, 1, 1]$.

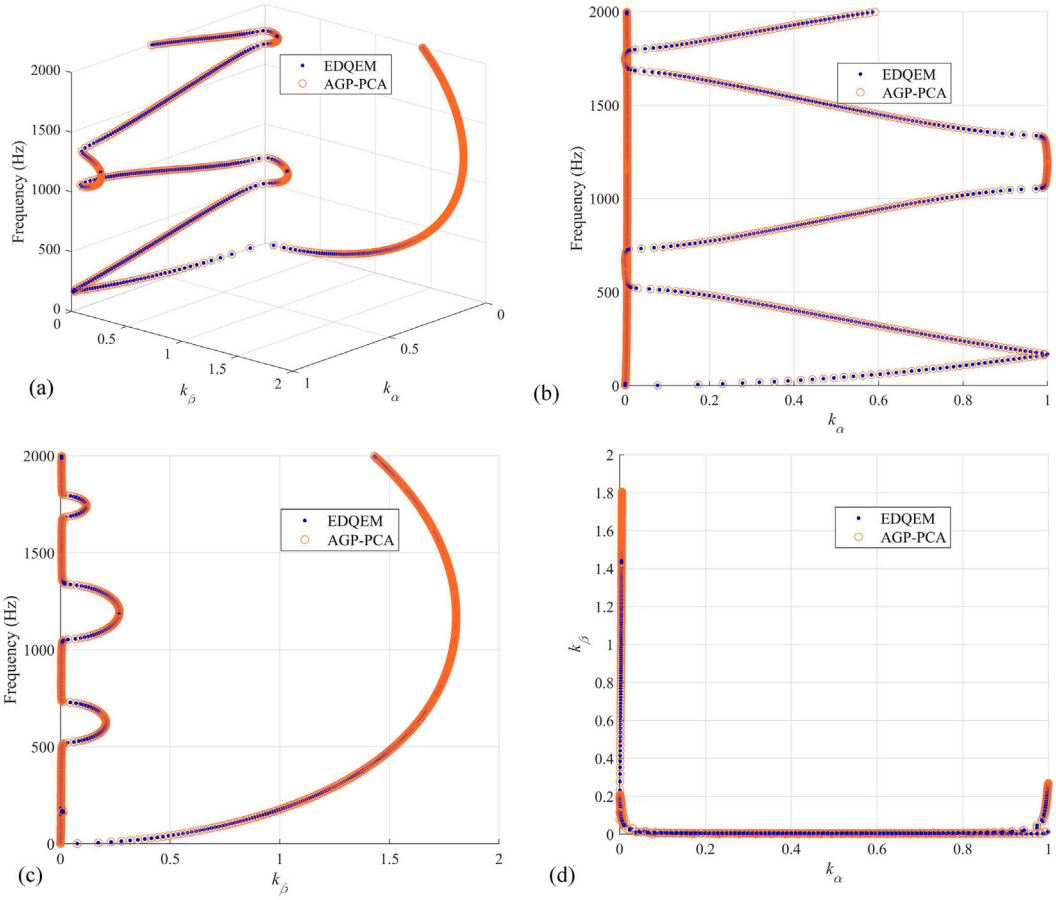

Fig. 13. (a) Complex dispersion relation of the damped periodic beam, (b) real dispersion curve (k_α vs. frequency) (c) imaginary dispersion curves (k_β vs. frequency) and (d) wavenumber components relationship (k_α vs. k_β) predicted by EDQEM and by AGP-PCA.

5. Further applications of the established AGP-PCA model

5.1. Uncertainty quantification of the complex dispersion relations

Due to its good accuracy and great efficiency, the established AGP-PCA model is applied to efficiently quantify the uncertainties in the complex dispersion relations and bandgap characteristics, resulting from the uncertainties in the inputs $\mathbf{x}$. In the current example, we consider the uncertainties in the geometrical properties. However, the approach can be applied to inputs that include uncertainties in not only geometrical properties but also material properties by defining corresponding $\mathbf{x}$. MCS is adopted here to propagate the uncertainties in $\mathbf{x}$ to investigate the impact of such uncertainties on the complex dispersion relations and bandgap characteristics. As an illustration, each x_i of the input vector $\mathbf{x}$ is assumed to follow a normal distribution with mean of 1 and standard deviation of 0.05. The number of MCS samples is selected as 500.

Fig. 14 shows the variability of the complex dispersion relations due to uncertainty in $\mathbf{x}$ calculated by EDQEM and by the AGP-PCA model. To clearly show each realization of the complex dispersion relation, the figure only shows 50 of the 500 realizations. In addition, the complex dispersion relation for $\mathbf{x} = [1, 1, 1]$ is also shown (corresponding to the darker lines). Qualitatively, Fig. 14(a) and (b) show close match. Based on the figures, it can be observed that in the low frequency range,

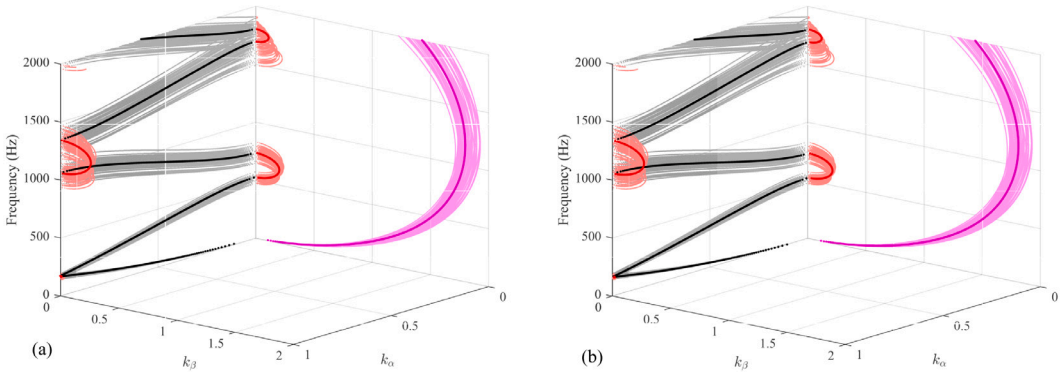

Fig. 14. Variability of the complex dispersion relations due to uncertainty in **x**, calculated by (a) EDQEM, and (b) AGP-PCA.

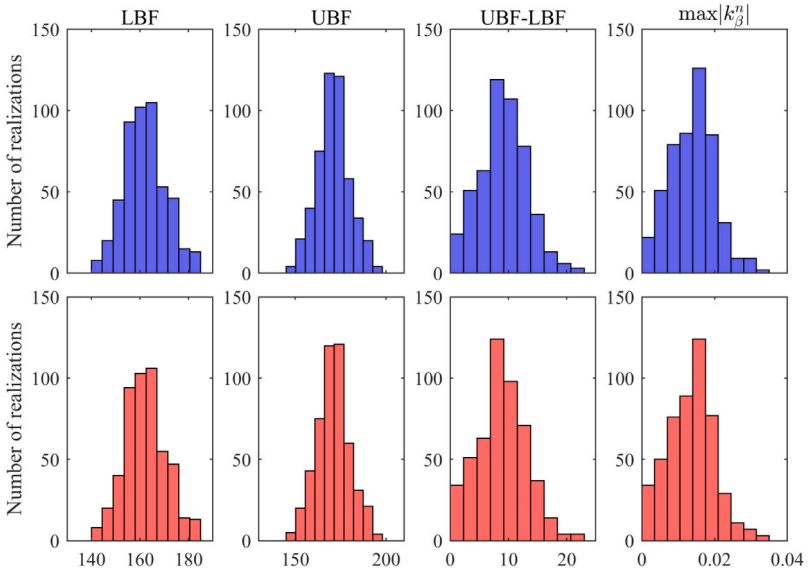

Fig. 15. Comparison of statistics of the first bandgap characteristics (i.e., LBF, UBF, UBF-LBF, and $\max|k_\beta^n|$) from EDQEM (upper) and AGP-PCA (lower).

the variability of the complex dispersion relations due to uncertainty in **x** is relatively smaller compared to that for the higher frequency range. Overall, uncertainty in **x** will have larger impact on the complex dispersion relation in the high frequency range. This is true for all the PE, P, and EE modes.

In terms of the bandgap characteristics, Figs. 15 and 16 show the histogram of the bandgap characteristics (i.e., LBF, UBF, UBF-LBF, and $\max|k_\beta^n|$) predicted by the AGP-PCA model for the first and second bandgaps, respectively. Note that the bandgap characteristics are extracted from each of the 500 realizations for the complex dispersion relations. For comparison purpose, results by the EDQEM are also shown in these figures. From the figures, observations can be made that the distributions of bandgap characteristics from the EDQEM and the AGP-PCA are close, which indicates accurate prediction of the bandgap characteristics. Table 2 further shows the mean μ and standard deviation σ values of the bandgap characteristics from the EDQEM and the AGP-PCA. Close match is observed between AGP-PCA and EDQEM for all the four bandgaps. In particular, even though the first bandgap is relatively narrow (with a bandgap of around 10 Hz), the established AGP-PCA model can accurately capture it. Overall, comparisons in the table further confirm the good prediction accuracy of the AGP-PCA model.

In terms of the computational efficiency, to run 500 simulations for uncertainty quantification, running the EDQEM model takes around 150 s for each simulation and total of 75,000 s, while the AGP-PCA model takes less than 0.5 s for all 500 simulations, corresponding to significant speedup. This speedup is of great importance to the uncertainty quantification of the complex dispersion relations and the bandgap characteristics, especially when the number of MCS samples is large, where directly using EDQEM (or other numerical models) would be computationally prohibitive.

Table 2
Comparison of bandgap characteristics from EDQEM and AGP-PCA.

Bandgap characteristics		LBF		UBF		$\max\|k_\beta^n\|$	
		μ	σ	μ	σ	μ	σ
$n=1$	EDQEM	161.8	8.5	170.9	8.9	0.0138	0.0061
	AGP-PCA	161.9	8.5	170.8	9.0	0.0135	0.0064
$n=2$	EDQEM	519.2	20.5	730.4	37.1	0.2083	0.0116
	AGP-PCA	519.3	20.4	730.3	37.2	0.2082	0.0117
$n=3$	EDQEM	1050.9	46.4	1335.8	54.9	0.2681	0.0129
	AGP-PCA	1051.1	46.2	1335.7	55.0	0.2677	0.0129
$n=4$	EDQEM	1682.9	78.7	1793.7	40.9	0.1171	0.0418
	AGP-PCA	1683.7	77.9	1793.4	41.5	0.1159	0.0403

5.2. Parameter study for the bandgap characteristics

Leveraging the good accuracy and great efficiency of the established AGP-PCA model, a parameter study is also carried out using AGP-PCA model to further investigate how the bandgap characteristics change with the variation in the inputs **x**.

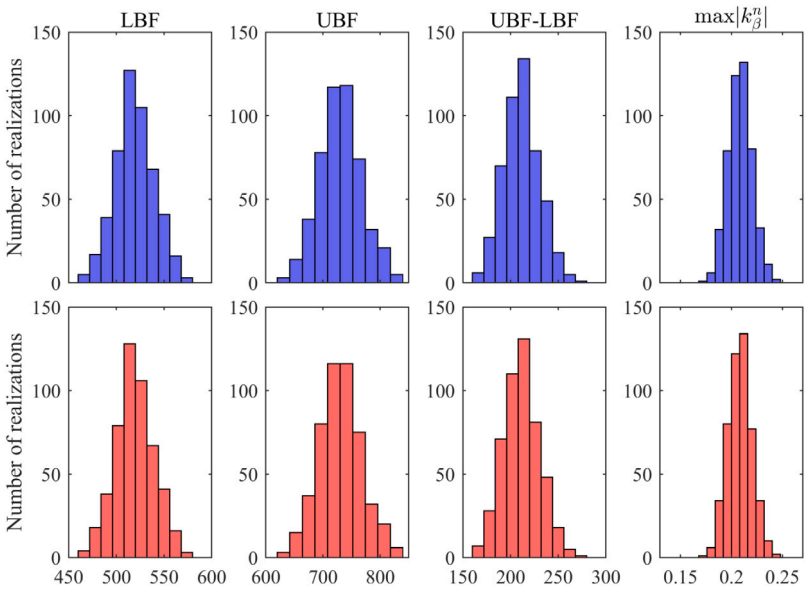

Fig. 16. Comparison of statistics of the second bandgap characteristics (i.e., LBF, UBF, UBF-LBF, and $\max|k_\beta^n|$) from EDQEM (upper) and AGP-PCA (lower).

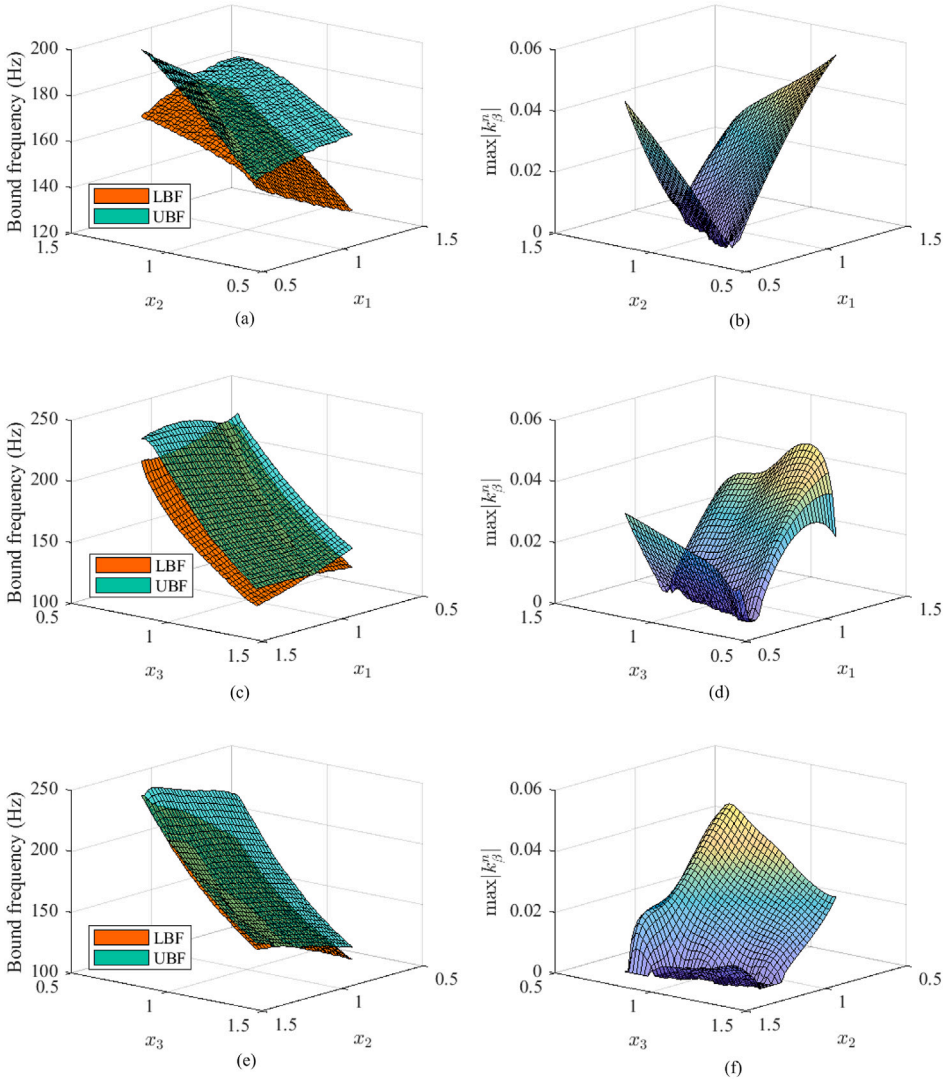

Fig. 17. Variation of the first bandgap characteristics versus (a) (b) x_1, x_2, (c) (d) x_1, x_3, and (e) (f) x_2, x_3 obtained by AGP-PCA.

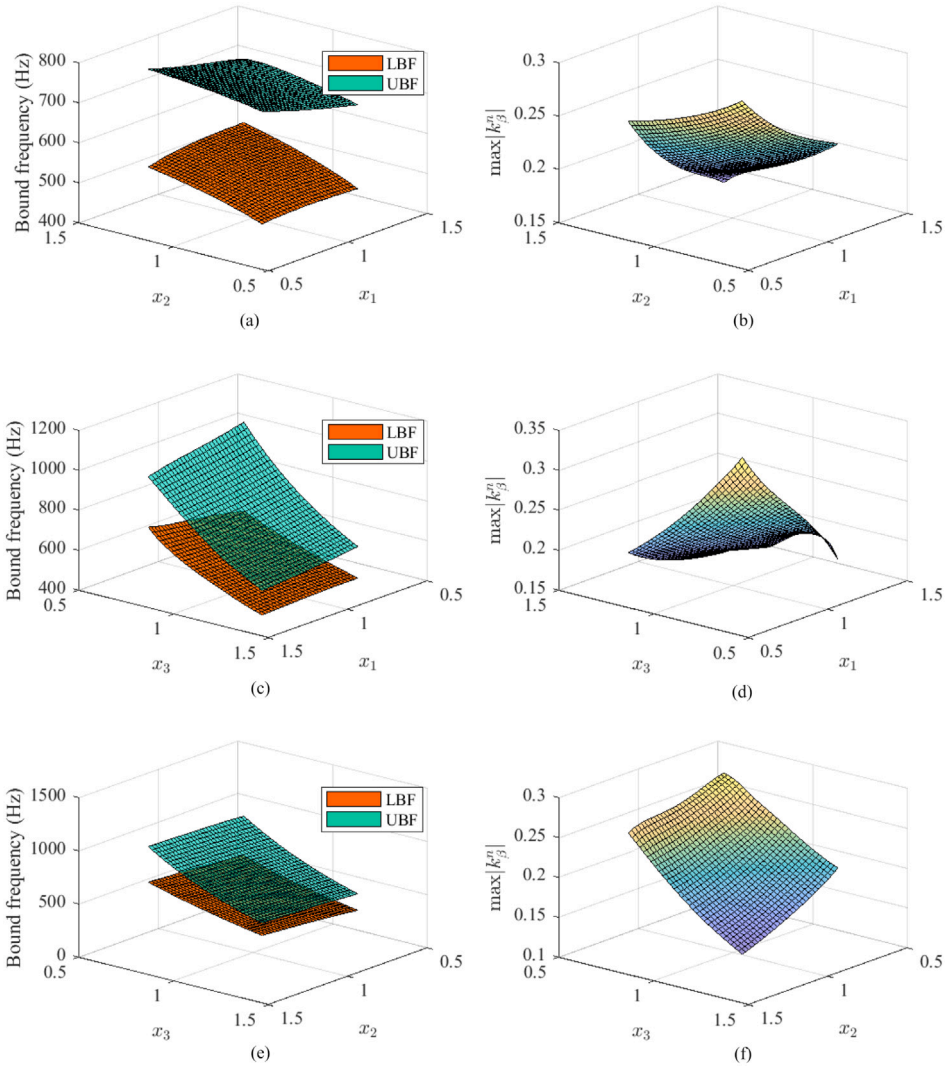

Fig. 18. Variation of the second bandgap characteristics versus (a) (b) x_1, x_2, (c) (d) x_1, x_3, and (e) (f) x_2, x_3 obtained by AGP-PCA.

Figs. 17 and 18 show the variation of the bandgap characteristics (i.e., LBF, UBF, and $\max|k_\beta^n|$) predicted by the AGP-PCA model for the first and second bandgaps with respect to variation of two of the inputs (with the other input fixed at 1). Overall the LBF, UBF and $\max|k_\beta^n|$ vary non-linearly with the three normalized geometrical parameters. Comparatively, it is observed that the width and the maximum attenuation parameter of the second bandgap are much larger than those of the first bandgap. In certain regions, the first bandgap is very narrow and even disappears. Thus, in the current case, the first bandgap is more sensitive to the variation of the geometrical parameters. Therefore, a proper design is needed to obtain a wider low-frequency bandgap. The fact that in certain regions the width of the first bandgap is zero further illustrates the challenges in directly building surrogate model for the bandgap characteristics due to the non-smooth nature of their variation.

On the other hand, in terms of computational effort, a thorough parametric investigation typically entails a large number of model evaluations. In this parametric study, a total of 2883 model evaluations are needed (the surface plot has interval of 0.02 for x_i), and the computation of the bandgap characteristics through the AGP-PCA model only takes around 10 s. By contrast, if the EDQEM method is applied to calculate the bandgap characteristics, the estimated computational time is at least 120 h. The significant difference of the computational cost between these two models further verifies the great efficiency of the AGP-PCA model in analysis, uncertainty quantification, and design of periodic structures when large number of model evaluations are required.

6. Conclusions

This paper proposed an adaptive Gaussian process (AGP) model to efficiently predict the complex dispersion relations for periodic structures with different properties. Instead of directly building GP for the dispersion relation, which is challenging due to the discontinuity in the dispersion relation and the high-dimensionality of the outputs, GP model is built for the coefficients of the dispersion equation that are continuous and smooth functions of the properties of the periodic structures. Based on the coefficients predicted by GP model, the dispersion equation is then analytically solved to establish the complex dispersion relations. Principal component analysis (PCA) is used to reduce the dimension of these coefficients and then the GP model is efficiently built with respect to the low-dimensional latent outputs. An adaptive sampling procedure using weighted accumulative errors (WAE) as infill criterion is integrated to iteratively add training data to effectively improve the GP model accuracy. Application to prediction and uncertainty quantification of the complex dispersion relations and bandgap characteristics for periodic beams demonstrates the high accuracy and efficiency of the proposed approach.

In the current paper, as an initial development of the proposed approach, to facilitate investigation of its various performances (e.g., comparison with results from numerical models, and comparison of uncertainty propagation results), a bi-component periodic beam was investigated, where the numerical model is relatively less expensive compared to more complex cases (e.g., two or three dimensional periodic structures). Future work will investigate the application and the performances of the proposed approach to two-dimensional problems where the complex dispersion relation becomes much more complex and the computational challenge is expected to be much higher than the EDQEM numerical model used here. The proposed approach in general has great promise in improving efficiency for uncertainty quantification, sensitivity analysis, and design optimization of periodic structures. Future work will also investigate the use of the proposed approach for optimization purpose where different adaptive sampling criterion needs to be used.

Declaration of competing interest

The authors declare that they have no known competing financial interests or personal relationships that could have appeared to influence the work reported in this paper.

Data availability

The raw/processed data required to reproduce these findings cannot be shared at this time as the data also forms part of an ongoing study.

Acknowledgments

Part of this research is sponsored by the Fundamental Research Funds for the Central Universities, China (2020JBM050), and the National Nature Science Foundation of China (51878031, 51878030). The authors Zhibao Cheng and Zhifei Shi would like to acknowledge this support. This research is supported in part by the National Science Foundation Engineering Design and System Engineering Program, USA under grant number CMMI-2034040. The authors Min Li and Gaofeng Jia would like to acknowledge this support.

References

Blatman, G., Sudret, B., 2010. Efficient computation of global sensitivity indices using sparse polynomial chaos expansions. Reliab. Eng. Syst. Saf. 95 (11), 1216–1229.
Bourinet, J.-M., Deheeger, F., Lemaire, M., 2011. Assessing small failure probabilities by combined subset simulation and support vector machines. Struct. Saf. 33 (6), 343–353.
Breitkopf, P., Naceur, H., Rassineux, A., Villon, P., 2005. Moving least squares response surface approximation: formulation and metal forming applications. Comput. Struct. 83 (17–18), 1411–1428.
Chen, Y., Huang, X., Sun, G., Yan, X., Li, G., 2017. Maximizing spatial decay of evanescent waves in phononic crystals by topology optimization. Comput. Struct. 182, 430–447.
Cheng, Z., Lin, W., Shi, Z., 2017. Dispersion differences and consistency of artificial periodic structures. IEEE Trans. Ultrason. Ferroelectr. Freq. Control 64 (10), 1591–1598.
Cheng, Z., Shi, Z., 2013a. Influence of parameter mismatch on the convergence of the band structures by using the Fourier expansion method. Compos. Struct. 106, 510–519.
Cheng, Z., Shi, Z., 2013b. Novel composite periodic structures with attenuation zones. Eng. Struct. 56, 1271–1282.
Cheng, Z., Shi, Z., Mo, Y.-L., 2018. Complex dispersion relations and evanescent waves in periodic beams via the extended differential quadrature method. Compos. Struct. 187, 122–136.
Cheng, Z., Shi, Z., Palermo, A., Xiang, H., Guo, W., Marzani, A., 2020. Seismic vibrations attenuation via damped layered periodic foundations. Eng. Struct. 211, 110427.
Dertimanis, V.K., Antoniadis, I.A., Chatzi, E.N., 2016. Feasibility analysis on the attenuation of strong ground motions using finite periodic lattices of mass-in-mass barriers. J. Eng. Mech. 142 (9), 04016060.
Forrester, A., Sóbester, A., Keane, A., 2008. Engineering Design via Surrogate Modelling: A Practical Guide. John Wiley & Sons.
Gao, N., Lu, K., 2020. An underwater metamaterial for broadband acoustic absorption at low frequency. Appl. Acoust. 169, 107500.
Jia, G., Shi, Z., 2010. A new seismic isolation system and its feasibility study. Earthq. Eng. Eng. Vib. 9 (1), 75–82.
Jia, G., Taflanidis, A.A., 2013. Kriging metamodeling for approximation of high-dimensional wave and surge responses in real-time storm/hurricane risk assessment. Comput. Methods Appl. Mech. Engrg. 261, 24–38.
Jia, G., Taflanidis, A.A., Nadal-Caraballo, N.C., Melby, J.A., Kennedy, A.B., Smith, J.M., 2016. Surrogate modeling for peak or time-dependent storm surge prediction over an extended coastal region using an existing database of synthetic storms. Nat. Hazards 81 (2), 909–938.
Jiang, P., Shu, L., Zhou, Q., Zhou, H., Shao, X., Xu, J., 2015. A novel sequential exploration-exploitation sampling strategy for global metamodeling. IFAC-PapersOnLine 48 (28), 532–537.
Jolliffe, I., 2011. Principal Component Analysis. Springer.
Jones, D., 2001. A taxonomy of global optimization methods based on response surfaces. J. Global Optim. 21, 345–383.
Kyprioti, A.P., Zhang, J., Taflanidis, A.A., 2020. Adaptive design of experiments for global kriging metamodeling through cross-validation information. Struct. Multidiscip. Optim. 1–23.
Laude, V., Achaoui, Y., Benchabane, S., Khelif, A., 2009. Evanescent Bloch waves and the complex band structure of phononic crystals. Phys. Rev. B 80, 092301.
Li, M., Cheng, Z., Jia, G., Shi, Z., 2019. Dimension reduction and surrogate based topology optimization of periodic structures. Compos. Struct. 229, 111385.
Li, M., Jia, G., 2020. Multifidelity Gaussian process model integrating low-and high-fidelity data considering censoring. J. Struct. Eng. 146 (3), 04019215.
Li, M., Wang, R.-Q., Jia, G., 2020. Efficient dimension reduction and surrogate-based sensitivity analysis for expensive models with high-dimensional outputs. Reliab. Eng. Syst. Saf. 195, 106725.
Lophaven, S.N., Nielsen, H.B., Søndergaard, J., 2002. DACE: a Matlab Kriging Toolbox. Technical Report No. IMM-TR-2002-12, Technical University of Denmark, Citeseer, Kongens Lyngby.
Lu, J., Zhan, Z., Apley, D.W., Chen, W., 2019. Uncertainty propagation of frequency response functions using a multi-output Gaussian process model. Comput. Struct. 217, 1–17.
Mace, B.R., Duhamel, D., Brennan, M.J., Hinke, L., 2005. Finite element prediction of wave motion in structural waveguides. J. Acoust. Soc. Am. 117 (5), 2835–2843.
Mace, B.R., Manconi, E., 2008. Modelling wave propagation in two-dimensional structures using finite element analysis. J. Sound Vib. 318 (4), 884–902.
Marelli, S., Sudret, B., 2015. Compressive polynomial chaos expansion for multi dimensional model maps. In: ICASP 2015: 12th International Conference on Applications of Statistics and Probability in Civil Engineering.
Moustapha, M., Bourinet, J.-M., Guillaume, B., Sudret, B., 2018. Comparative study of kriging and support vector regression for structural engineering applications. ASCE-ASME J. Risk Uncertain. Eng. Syst. A Civ. Eng. 4 (2), 04018005.
Palermo, A., Krödel, S., Matlack, K.H., Zaccherini, R., Dertimanis, V.K., Chatzi, E.N., Marzani, A., Daraio, C., 2018. Hybridization of guided surface acoustic modes in unconsolidated granular media by a resonant metasurface. Phys. Rev. A 9, 054026.
Rasmussen, C.E., Williams, C.K.I., 2006. Gaussian Processes for Machine Learning. MIT Press, Cambridge, Mass..
Sacks, J., Welch, W., Mitchell, T., Wynn, H., 1989. Design and analysis of computer experiments. Statist. Sci. 4 (4), 409–435.
Schneider, F., Papaioannou, I., Ehre, M., Straub, D., 2020. Polynomial chaos based rational approximation in linear structural dynamics with parameter uncertainties. Comput. Struct. 233, 106223.
Simpson, T.W., Poplinski, J., Koch, P.N., Allen, J.K., 2001. Metamodels for computer-based engineering design: survey and recommendations. Eng. Comput. 17 (2), 129–150.
Sudret, B., 2008. Global sensitivity analysis using polynomial chaos expansions. Reliab. Eng. Syst. Saf. 93 (7), 964–979.
Taflanidis, A.A., Jia, G., Kennedy, A.B., Smith, J.M., 2013. Implementation/optimization of moving least squares response surfaces for approximation of hurricane/storm surge and wave responses. Nat. Hazards 66 (2), 955–983.
Tang, D., Pang, F., Zhang, Z., Li, L., 2021. Flexural wave propagation and attenuation through timoshenko beam coupled with periodic resonators by the method of reverberation-ray matrix. Eur. J. Mech. A Solids 86, 104153.
Thierry, V., Brown, L., Chronopoulos, D., 2018. Multi-scale wave propagation modelling for two-dimensional periodic textile composites. Composites B 150, 144–156.
Tipping, M., Bishop, C., 1999. Probabilistic principal component analysis. J. R. Stat. Soc. Ser. B Stat. Methodol. 61 (3), 611–622.
Veres, I.A., Berer, T., 2012. Complexity of band structures: Semi-analytical finite element analysis of one-dimensional surface phononic crystals. Phys. Rev. B 86, 104304.
Wenzel, M., Bursi, O.S., Antoniadis, I., 2020. Optimal finite locally resonant metafoundations enhanced with nonlinear negative stiffness elements for seismic protection of large storage tanks. J. Sound Vib. 115488.
Xiao, Y., Wen, J., 2020. Closed-form formulas for bandgap estimation and design of metastructures undergoing longitudinal or torsional vibration. J. Sound Vib. 485, 115578.

Xiao, Y., Wen, J., Wen, X., 2012. Flexural wave band gaps in locally resonant thin plates with periodically attached spring–mass resonators. J. Phys. D: Appl. Phys. 45 (19), 195401.

Yaghoubi, V., Marelli, S., Sudret, B., Abrahamsson, T., 2017. Sparse polynomial chaos expansions of frequency response functions using stochastic frequency transformation. Probab. Eng. Mech. 48, 39–58.

Yao, Z., Zhao, R., Zega, V., Corigliano, A., 2020. A metaplate for complete 3D vibration isolation. Eur. J. Mech. A Solids 84, 104016.

Zhang, J., Taflanidis, A., Medina, J., 2017. Sequential approximate optimization for design under uncertainty problems utilizing kriging metamodeling in augmented input space. Comput. Methods Appl. Mech. Engrg. 315, 369–395.

Zhang, J., Taflanidis, A.A., Nadal-Caraballo, N.C., Melby, J.A., Diop, F., 2018. Advances in surrogate modeling for storm surge prediction: storm selection and addressing characteristics related to climate change. Nat. Hazards 94 (3), 1225–1253.

Zhou, W., Muhammad, Chen, W., Chen, Z., Lim, C., 2019. Actively controllable flexural wave band gaps in beam-type acoustic metamaterials with shunted piezoelectric patches. Eur. J. Mech. A Solids 77, 103807.